



ОБЪЕДИНЕННЫЙ ИНСТИТУТ ЯДЕРНЫХ ИССЛЕДОВАНИЙ JOINT INSTITUTE FOR NUCLEAR RESEARCH

2[65]-94

JINR RAPID COMMUNICATIONS

# Объединенный институт ядерных исследований Joint Institute for Nuclear Research

2[65]-94

# JINR RAPID COMMUNICATIONS

сборник collection



Дубна 1994

# ОГЛАВЛЕНИЕ CONTENTS

О-Меter Theory  Ю.Ф.Киселев, К.М.Дулиа, Т.О.Нииникоски  Теория Q-метра	. 5
A.M.Baldin, Kh.U.Abraamyan, S.V.Afanasiev, Yu.S.Anisimov, V.V.Arkhipov, A.S.Artyomov, V.V.Avdeichikov, V.K.Bondarev, A.F.Elishev, A.Yu.Isupov, V.A.Kashirin, A.N.Khrenov, V.I.Kolesnikov, A.D.Kovalenko, V.A.Kuznetsov, A.G.Litvinenko, A.I.Malakhov, P.K.Maniakov, E.A.Matyushevsky, G.L.Melkumov, I.I.Migulina, A.S.Nikiforov, V.A.Nikitin, P.V.Nomokonov, V.G.Perevozchikov, S.G.Reznikov, I.A.Rufanov, A.Yu.Semenov, V.A.Smirnov, P.I.Zarubin, I.Atanasov, V.N.Penev, A.I.Berlev, V.A.Krasnov, A.I.Maevskaia, S.V.Zadorozhny An Experimental Run	
оп the New Superconducting Accelerator Nuclotron at 3.8 and 6.2 GeV/c Deuteron Momentum  А.М.Балдин, Х.У.Абраамян, С.В.Афанасьев, Ю.С.Анисимов, В.В.Архипов, А.С.Артемов, В.В.Авдейчиков, В.К.Бондарев, А.Ф.Елишев, А.Ю.Исупов, В.А.Каширин, А.Н.Хренов, В.И.Колесников, А.Д.Коваленко, В.А.Кузнецов, А.Г.Литвиненко, А.И.Малахов, П.К.Маньяков, Е.А.Матюшевский, Г.Л.Мелкумов, И.И.Мигулина, А.С.Никифоров, В.А.Никитин, П.В.Номоконов, В.Г.Перевозчиков, С.Г.Резников, И.А.Руфанов, А.Ю.Семенов, В.А.Смирнов, П.И.Зарубин, И.Атанасов, В.Н.Пенев, А.И.Берлев, В.А.Краснов, А.И.Маевская, С.В.Задорожный Эксперимент на новом сверхпроводящем ускорителе Нуклотрон при импульсе дейтронов 3,8 и 6,2 ГэВ/с	26
A.A.Baldin, L.G.Efimov, G.A.Feofilov, S.N.Filippov, V.S.Pantuev, F.F.Valiev  Some Results of MCP Timing Resolution Measurements with Minimum Ionizing Particles  А.А.Балдин, Л.Г.Ефимов, Г.А.Феофилов, С.Н.Филиппов, В.С.Пантуев, Ф.Ф.Валиев	

Некоторые результаты измерений временного разрешения МКП
для минимально ионизирующих частиц
Н.Ангелов, В.Б.Любимов, Р.Тогоо Кластеризация в процессах множественного рождения частиц в ядрах. Двухкластерные корреляции N.Angelov, V.B.Lyubimov, R.Togoo Clusterization in Processes of Multiple Particle Production in Nuclei.
Two-Cluster Correlations
S.V.Goloskokov, O.V.Selyugin The A <sub>LL</sub> Asymmetry in Diffractive Reactions and Structure of Quark-Pomeron Vertex C.В.Голоскоков, О.В.Селюгин A <sub>LL</sub> -асимметрия в дифракционных реакциях и структура кварк-померонной вершины 48
М.П.Иванов, И.В.Кузнецов, В.Ф.Кушнирук, В.С.Саламатин, Ю.Г.Соболев, Г.В.Букланов Выходы и энергетические спектры ядер Не, Li, Ве в спонтанном делении <sup>248</sup> Cm M.P.Ivanov, I.V.Kuznetsov, V.F.Kushniruk, V.S.Salamatin, Yu.G.Sobolev, G.V.Buklanov The Yields and Energy Spectra of He, Li and Be Nuclei
in <sup>248</sup> Cm Spontaneous Fission

#### **Q-METER THEORY**

Yu.F.Kisselev<sup>1</sup>, C.M.Dulya<sup>2</sup>, T.O.Niinikoski<sup>3</sup>

This paper develops the theory of series Q-meters used for measurements of NMR signals. For the first time we have derived closed form expressions for the nuclear susceptibility in terms of the Q-meter output voltage and for the residual Q-curve. We discuss the corrections involved in measuring nuclear polarization from NMR signals by using signals for the deuteron and proton as examples. Deuteron signals are shown to contain a false asymmetry, while proton signals have substantial distortions due to the long signal wings and the depth of modulation. Moreover, for the first time the importance of making a phase correction is demonstrated. We conclude that the series Q-meter with real part detection is not sufficient to produce an output voltage from which the nuclear susceptibility can be determined and thus an additional phase-sensitive detector is necessary for obtaining the imaginary part of the signal as well.

The investigation has been performed at CERN, Geneva.

#### **Теория** *Q*-метра

#### Ю.Ф.Киселев, К.М.Дулиа, Т.О.Нииникоски

В работе осуществлено дальнейшее развитие теории последовательного *Q*-метра, прибора для измерения ядерной поляризации мишеней. Впервые получено выражение для ядерной восприимчивости мишени через выходное напряжение *Q*-метра. Обсуждается коррекция NMR протонных и дейтронных сигналов, используемых при измерении поляризации. Показано, что дейтронные сигналы содержат ложную асимметрию. Протонные сигналы существенно искажены дисперсионной компонентой при большой глубине модуляции. Демонстрируется важность нового типа фазовой коррекции. Анализ показывает, что последовательный *Q*-метр с детектором реальной компоненты сигнала не позволяет восстановить ядерную восприимчивость. Чтобы решить эту проблему, требуется дополнительный фазовый детектор мнимой компоненты сигнала.

Работа выполнена в ЦЕРН, Женева.

#### 1. Introduction

The series Q-meter has found wide acceptance for the measurement of NMR spectra, especially in the precise measurement of nuclear polarization in polarized targets used in scattering experiments. Theoretical treatments

<sup>&</sup>lt;sup>1</sup>Permanent address: Laboratory of Particle Physics, Joint Institute for Nuclear Research, Dubna, Moscow Region, Russia

<sup>&</sup>lt;sup>2</sup>University of California, Department of Physics, Los Angeles CA 90024, USA

<sup>&</sup>lt;sup>3</sup>CERN, CH-1211 Geneva 23, Switzerland

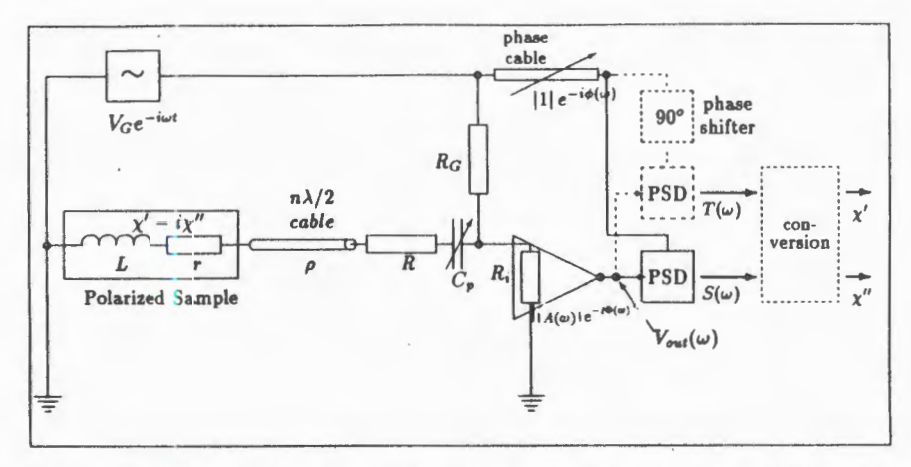


Fig.1. This is a block diagram of the Q-meter circuit detecting the real part of the NMR signal. The dashed lines correspond to the additions necessary to correct the Q-meter output signal such that the new outputs become proportional to the nuclear polarization

[1,2,3] have, until now, centered on approximate solutions of the equations for the Q-meter output voltage based on expansions in terms of the nuclear susceptibility using circuit elements as parameters. In this paper, we express the susceptibility as a function of the circuit parameters and the Q-meter output voltage and, furthermore, demonstrate general properties of the relationship between the Q-meter output signal and the susceptibility.

The sensing probe of the Q-meter circuit, shown on Fig.1, is a coil embedded in the material under study which couples inductively with the magnetic moments of the nuclei in that material. As a result of this interaction, the coil impedance  $Z_L$  varies linearly with the complex magnetic susceptibility  $\chi(\omega)$  of the material according to 1

$$Z_{I} = r + i\omega L (1 + \eta \chi (\omega)), \tag{1}$$

where  $\omega=2\pi\nu$ ,  $\nu$  is the frequency of the rf generator,  $\eta$  is the effective filling factor of the material in the coil and L is the inductance of the NMR coil when  $\chi=0$ . The complex function  $\chi(\omega)=\chi'(\omega)-\iota\chi''(\omega)$  is the nuclear susceptibilty of the material; its real part is called dispersion; and the imaginary part, absorption. The susceptibility is finite for all frequencies, but the dispersion changes the sign; it tends to have larger values in the vicinity of the Larmor frequency. The absorption describes the spectral distribution

In MKSA umits

of spins near the NMR Larmor frequency and its integral is proportional to the nuclear polarization. The constant of proportionality may be found by measuring the signal for samples in thermal equilibrium (TE) in a known magnetic field and temperature. In this case, the polarization is calculable from the Maxwell — Boltzmann distribution and is described by the Brillouin function.

In the Q-meter, the coil is usually connected to a room-temperature tuning capacitor and amplifier by a coaxial transmission line whose length is adjusted to an integer number of half-wavelengths at the Larmor frequency. These form a hybrid series tuned circuit [1]. Given the electrical parameters of the receiver circuitry and a well-defined NMR line shape, it is not difficult to calculate the Q-meter output voltage. In practice, however, we wish to solve exactly the opposite problem; namely to evaluate the complex magnetic susceptibility from the Q-meter signal. In this paper, we will review the theory of the Q-meter and apply these ideas to specific examples for proton and deuteron signals.

## 2. The Q-Meter Circuit

Since we are mainly concerned with series Q-meters using rf phase sensitive signal detection and homodyne receiver circuitry [4,5] as in Fig.1, we will incorporate the following definitions and values for the circuit parameters now:

**Table of Circuit Parameters** 

Para- meter	Description of parameter		Typical value	
		Units	Proton	Deuteron
ν <sub>0</sub>	Larmor frequency	[MHz]	106.5	16.35
$\Delta \nu$	Range of frequency sweep	[kHz]	600	500
$R_G$	Feed resistance	[Ω]	900	900
R	Damping resistance	[Ω]	33	9
Ri	Amplifier input impedance	[Ω]	120	50
r	Coil resistance	[Ω]	0.3	0.3
$C_p$	Tuning capacitance	[pF]	19	:200
L	Coil inductance	[µH]	0.091	().48
ρ	Cable impedance	[Ω]	50	:50
ε	Cable dielectric constant		2	22
α	Cable attenuation constant	[Np/m]	0.02	().005
β	Cable phase constant $\beta = \omega \sqrt{\varepsilon/c}$	[m <sup>-1</sup> ]		

Para- meter	Description of parameter	Units	Typical value	
			Proton	Deuteron
l	Cable length $l = nc/2v_0\sqrt{\varepsilon}$	[m]	4.99	6.42
n	Number of cable half wavelengths		5	1
С	Speed of light	[m/s]	2.9979 · 108	2.9979 - 10
$V_G$	Voltage of high frequency synthesizer	[V]	0.1	0.1
$A(\omega)$	Gain of high frequency amplifier		50	50

The output of the amplifier is connected to the input of a phase sensitive detector (PSD). The PSD selects the real part of the voltage at its input terminal relative to a reference voltage. This is the main idea of the Liverpool Q-meter [5]. In our conclusions, we will suggest the improvement of this Q-meter design by adding another PSD for selecting the imaginary part of the signal as well as the real part. Moreover, we also suggest a function that will transform the output voltage to be proportional to the complex nuclear susceptibility.

# 3. Determination of the Nuclear Susceptibility from the Q-Meter Signal

The nuclear polarization is proportional to the integral of the absorption, where the limits of integration are usually restricted to frequencies near the Larmor frequency (see Section 6). In other words, the polarization is given by

$$P = C \int_{\omega_{\min}}^{\omega_{\max}} \chi''(\omega) d\omega, \qquad (2)$$

where C is a constant determined from calibration at TE. To calculate the polarization we thus need to know the absorption spectrum. Thus, one would like to write an equation for the susceptibility as a function of the Q-meter output voltage.

The Q-meter output voltage, which is the complex voltage at the output of the rf amplifier, is a function of the nuclear susceptibility. However, the effective filling factor of the coil,  $\eta$ , from Eq.(1) disappears for relative values of the polarization. Thus, we will define and calculate a complex function  $\xi(\omega) := \eta \chi(\omega)$ . The general expressions for the Q-meter output voltage [1,3] can be written in complex form [6] as

$$V_{\text{out}}(\omega) = \frac{V_n}{R_C} \frac{Z(\xi)}{1 + pZ(\xi)},$$
(3)

where  $Z(\xi)$  is the resonant circuit impedance

$$Z(\xi) = R - \frac{\iota}{\omega C_p} + \frac{\rho^2 \tanh(\gamma l) + \rho \left[r + \iota \omega L(1 + \xi)\right]}{\rho + \left[r + \iota \omega L(1 + \xi)\right] \tanh(\gamma l)},$$
 (4)

with

$$p = \frac{1}{R_i} + \frac{1}{R_G}$$
,  $V_n = A(\omega)V_G$  and  $\gamma = \alpha + \iota\beta$ , (5)

where  $\gamma$  is the complex propagation constant of the coaxial transmission line and  $\alpha$  is its average attenuation constant. The coefficient p is the admittance due to the feed and the shunt resistances  $R_G$  and  $R_i$ . Table 1 describes the circuit parameters and gives their numerical values used in our estimations.

If the generator frequency is swept slowly enough so that  $\xi(\omega)$  has no explicit time dependence, then the normalized Q-meter output voltage from Eq. (3).

$$\frac{V_{\text{out}}(\xi)}{V_n} = \frac{Z_{\text{eff}}}{R_G} = \frac{1}{R_G} \frac{Z(\xi)}{1 + pZ(\xi)} = S_{\text{eff}}(\xi) + \iota T_{\text{eff}}(\xi)$$
(6)

can be considered an equivalent circuit impedance,  $Z_{\rm eff}$ , of a two terminal, divided by the damping resistance  $R_G$ . In other words, using the general properties of two terminal relations [7], we can calculate the imaginary part of the Q-meter output voltage from the real part by using the Kramers — Kronig relation [7] for an impedance. Thus,

$$\frac{V_{\text{out}}(\omega)}{V_n} = S_{\text{eff}}(\omega) + \iota \frac{2\omega}{\pi} \mathcal{P} \int_0^\infty \frac{S_{\text{eff}}(\omega') d\omega'}{{\omega'}^2 - \omega^2}, \tag{7}$$

where  $S_{\rm eff}>0$  for both signs of nuclear polarization and  $\mathcal P$  means that the principal value of the integral be taken. In addition, the Kramers — Kronig relation can be formally applied to the difference of two impedances measured at  $\xi \neq 0$  and  $\xi = 0$  just as well as to Eq. (7). This difference

$$\frac{\Delta V_{\text{out}}(\omega)}{V_n} = \frac{V_{\text{out}}(\xi) - V_{\text{out}}(\xi = 0)}{V_n} = S(\omega) + \iota T(\omega) = 
= S(\omega) + \iota \frac{2\omega}{\pi} \mathcal{P} \int_0^\infty \frac{S(\omega')d\omega'}{{\omega'}^2 - \omega^2},$$
(8)

where

$$S(\omega) = S_{\text{eff}}(\xi) - S_{\text{eff}}(\xi = 0), \qquad S(\omega) < 0 \text{ or } S(\omega) > 0$$
 (9)

and

$$T(\omega) = T_{\text{eff}}(\xi) - T_{\text{eff}}(\xi = 0),$$
 (10)

will be called the NMR signal because its real part,  $S(\omega)$ , and its imaginary part,  $T(\omega)$ , are nearly proportional to the imaginary (absorption) and real (dispersion) parts of the nuclear susceptibility, respectively. The real part of the NMR signal,  $S(\omega)$ , can be either positive or negative owing to the fact that it is the difference of two independent measurements. Using Eqs. (3,4,8) we get the NMR signal in terms of the circuit impedance Z

$$\frac{\Delta V_{\text{out}}(\omega)}{V_n} = \frac{1}{R_G} \frac{Z(\xi) - Z(\xi = 0)}{[1 + pZ(\xi)][1 + pZ(\xi = 0)]}.$$
 (11)

Then by defining a frequency-dependent complex function

$$G(\omega) = \rho^{-1} [1 + pZ_I(\xi = 0)] [\rho + (r + \iota \omega L) \tanh(\gamma l)] \cosh(\gamma l)$$
 (12)

we find the normalized NMR signal as

$$S(\omega) + iT(\omega) = \frac{\Delta V_{\text{out}}(\omega)}{V_n} = \frac{1}{R_G G(\omega)} \times \frac{i\omega L \xi}{G(\omega) + \rho^{-1} i\omega L \xi \cosh(\gamma l) \left\{ p\rho + \left[ 1 + p(R - \iota/\omega C_p) \right] \tanh(\gamma l) \right\}}$$
(13)

and thereby the equation for  $\xi(\omega)$  in closed form is [6]

$$\xi(\omega) = \eta \left\{ \chi'(\omega) - \iota \chi''(\omega) \right\} = \frac{-\iota R_G G^2(\omega)}{\omega L} \times \frac{\left\{ \Delta V_{\text{out}}(\omega) / V_n \right\}}{1 - \rho^{-1} R_G G(\omega) \cosh(\gamma l) \left\{ p\rho + \left[ 1 + p(R - \iota / \omega C_p) \right] \tanh(\gamma l) \right\} \left\{ \Delta V_{\text{out}}(\omega) / V_n \right\}},$$
(14)

where  $\Delta V_{\rm out}(\omega)/V_n$  (not to be confused with the modulation, M) is described by Eq.(8). According to Eq.(14), the actual NMR signals have to be transformed by a complex function to obtain the output signal as a linear function of nuclear susceptibility (see Fig.1).

It follows from the Kramers — Kronig relation for the susceptibility that the solution to Eq.(14) must satisfy the equation [8]

$$\xi'(\omega) - \xi_{\omega}' = \frac{2}{\pi} \mathcal{P} \int_{0}^{\infty} \frac{\omega' \xi''(\omega') d\omega'}{{\omega'}^2 - \omega^2}$$
 (15)

which is the condition for self-consistency of the experimental data. If the signal wings are cut, then the imaginary part of the Q-meter signal cannot be accurately calculated by Eq.(8). Hence, an error is produced in the calculation of the susceptibility from Eq.(14), and in this case Eq.(15) will no longer be satisfied. We therefore propose that the real and imaginary parts of the Q-meter signal be measured, thus to avoiding any complications of using Eq.(8) in calculating  $\xi'(\omega)$  via Eq.(14).

#### 4. Discussion

Let us discuss the difference between the use of  $S(\omega)$  and  $\chi''(\omega)$  of Eq.(14) in determining the polarization from the integrated spectra. It has been shown [1,2,3] that the nuclear polarization is given approximately by

$$P \approx C \int_{\omega_{\min}}^{\omega_{\max}} S(\omega) d\omega, \qquad (16)$$

where the integral is taken over the width  $\omega_{\text{max}} - \omega_{\text{min}}$  of the frequency sweep. Comparing Eqs. (2,14,16) we come to the following conclusions:

- 1. The term  $\xi(\omega)$  in the denominator of Eq.13 describes the experimentally observed difference in the form of the proton NMR line shape between opposite signs of polarization. We will calculate this distortion later in Section 4.2. The term  $\Delta V_{\rm out}(\omega)/V_n$  in the denominator of Eq.(14) allows one to find back  $\chi(\omega)$  without distortions from the experimental signal.
- 2. Eq. (16) does not take into account the frequency dependence, causes a distortion for wide signals, most notably the false asymmetry of the deuteron signals. It can be shown, however, that the integral of a distorted signal  $S(\omega)$  represents to a good approximation the polarization (Section 4.2).
- 3. Eq. (16) does not take into account the distortion of NMR signals due to phase errors. It causes, via  $V_n(\omega)$  (see Eq.6), an additional mixing of  $\xi'(\omega)$  and  $\xi''(\omega)$  in Eq. (14), and thus this effect cannot be accounted for unless both the real and imaginary parts of the Q-meter output voltage are measured (Section 4.4).

## 4.1. The First Order Expansion

A first order solution can be found by a complex series expansion of Eqs. (3,4) about  $\xi(\omega) = 0$ . Alternatively, we find the first order approximation to  $\xi(\omega)$  by setting  $\Delta V_{\rm out}(\omega)/V_n = 0$  in the denominator of Eq. (14) giving

$$\xi''(\omega) + \iota \xi'(\omega) = G^2(\omega) \left( \frac{R_G}{\omega L} \right) \left\{ \frac{\Delta V_{\text{out}}(\omega)}{V_n} \right\}, \tag{17}$$

where  $\Delta V_{\text{out}}(\omega)/V_n$  as

$$\xi'(\omega) = \frac{R_G}{\omega L} \left\{ \operatorname{Im} \left( G^2 \right) S(\omega) + \operatorname{Re}(G^2) T(\omega) \right\}$$
 (18)

and

$$\xi''(\omega) = \frac{R_G}{\omega L} \left\{ \text{Re} \left( G^2 \right) S(\omega) - \text{Im}(G^2) T(\omega) \right\}. \tag{19}$$

If only the real part of the Q-meter signal is measured, then  $T(\omega)$  is obtained from Eq.(8). Thus, in the linear approximation, the integral of the real part of the output voltage over the frequency sweep as in Eq.(16) is generally proportional to the nuclear polarization, since although according to Eqs.(18) and (19)  $S(\omega)$  contains frequency dependent coefficients, these are independent of the polarization. However, the integral of  $T(\omega)$  of Eq.(19) is non zero especially in the case of high polarized deuterons with asymmetric signals. For narrow symmetric signals, however, this proportionality is well obeyed even if the line shape  $\xi''(\omega)$  changes as a function of the polarization.

# 4.2. The Line Shape Distortion of Proton Signals

We estimate the line shape distortion for protons from Eq.(14) with the values  $\gamma l = 5\pi \iota$ ,  $\tanh(\gamma l) = 0$ ,  $G(\omega) \cosh(\gamma l) = 1$ ,  $pR_G = 8.5$ . The denominator of Eq.(14) becomes

$$1 - \rho^{-1} R_{G}G(\omega) \cosh(\gamma l) \left\{ p\rho + \left[ 1 + p \left( R - \frac{\iota}{\omega C_{p}} \right) \right] \tanh(\gamma l) \right\} \left\{ \frac{\Delta V_{\text{out}}(\omega)}{V_{n}(\omega)} \right\} \approx 1 - pR_{G} \left\{ \frac{\Delta V_{\text{out}}(\omega)}{V_{n}} \right\} \approx 1 - 8.5 \left\{ \frac{\Delta V_{\text{out}}(\omega)}{V_{n}(\omega)} \right\}, \tag{20}$$

where  $V_n = V_G A(\omega) \approx 5$  V. Consequently, the following equation, valid for the region near the Larmor frequency ( $\xi' = 0$ ), is obtained for the output sig-

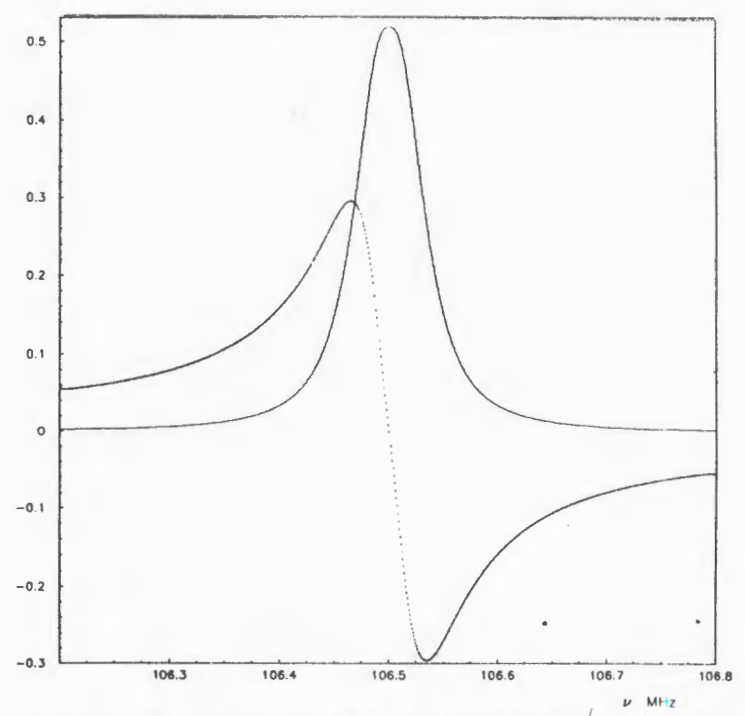


Fig. 2. The dotted line shows the dispersion,  $\xi'(\omega)$ , and the solid line shows the absorption,  $\xi''(\omega)$ . These are the imaginary and real outputs of the Q-meter, respectively, after making a transformation by Eq. (14) using the proposed additions to the Q-meter shown in Fig. 1. The line shape for the absorption signal is the modified lorentzian function  $\xi''(\omega) \sim$ 

$$\sim \left[1 + \left|\frac{\omega - \omega_0}{\sigma}\right|^{2.54}\right]^{-1}$$
 found in [9]

nal for both positive and negative polarizations (sign of  $\Delta V_{\text{out}}(\omega)$ ) for any frequency tuned cable ( $\gamma l = 5\pi \iota$ )

$$\xi''(\omega) = \frac{9.7 \left\{ \Delta V_{\text{out}}(\omega) / V_n(\omega) \right\}}{1 - 8.5 \left\{ \Delta V_{\text{out}}(\omega) / V_n(\omega) \right\}}.$$
 (21)

Eqs. (20, 21) clearly show that the distortion as well as the nonlinearity of the output signal depend on the amplitude of the Q-meter output voltage and the shunting resistances  $R_i$  and  $R_G$ .

In order to better demonstrate the distortion of the proton signal shape we simulate the absorption part of the proton susceptibility by a Lorentzian-

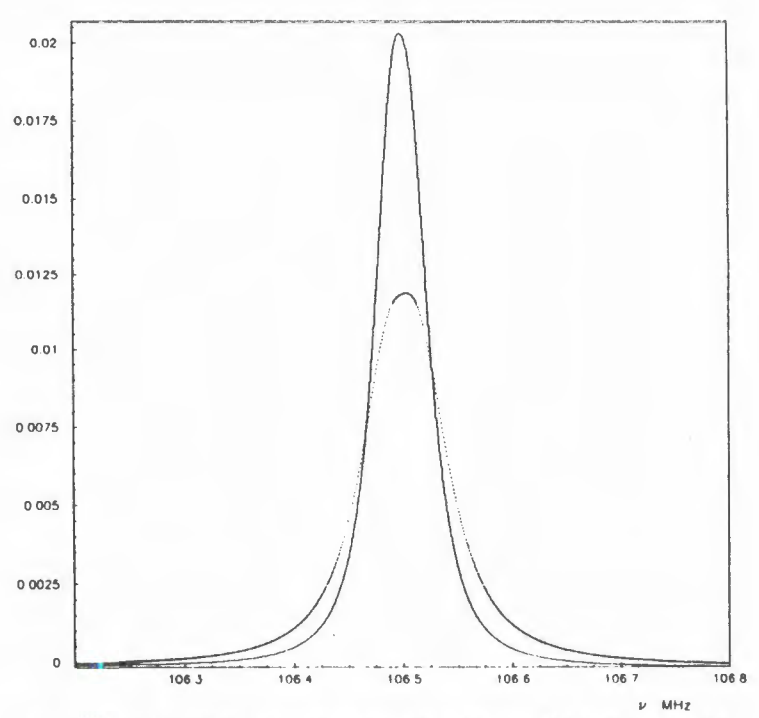


Fig. 3. This plot shows the line shape distortion of the real part of proton signals for the same but opposite signs polarization. The modulation is 0.30 for the positive signal and -0.38 for the negative signal. The solid line is the Q-meter signal for negative polarization and the dotted line is for positive polarization. The susceptibility has an original width of 70.0 kHz at FWHM. The positive signal is broadened to 76.0 kHz at FWHM while the negative signal is narrowed to 62.0 kHz at FWHM

like function found in [9]. The dispersion is then calculated from Eq.(15) using the algorithm of Sperisen [10]; this is shown in Fig.2. The constant  $\eta \chi_0$  is adjusted to give the desired value of the modulation (M). The simulation calculates the Q-meter output signal as a function of the susceptibility from Eqs. (3,4). The results are plotted in Figs.3,4. For the same but opposite sign of polarization, that is the same but opposite sign of susceptibility, we calculate the Q-meter output voltage and find that the positive polarization Q-meter signal (M = 0.30) is broadened to 76.0 kHz at FWHM whereas the negative polarization Q-meter signal (M = -0.38) is narrowed to 62.0 kHz at FWHM with respect to the width of the susceptibility of 70.0 kHz at FWHM. The proton signal amplitude is larger for negative polarization than

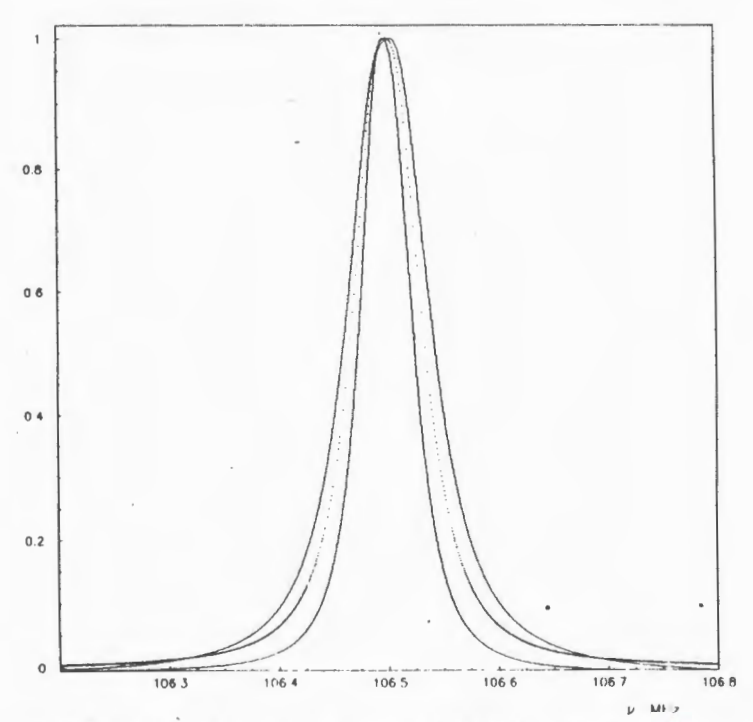


Fig. 4. Same as Fig. 3 except the Q-meter signals and absorptions have been normalized in order to highlight the line shape distortions. The widest line is the Q-meter signal for positive polarization, the narrowest line is the Q-meter signal for negative polarization and the middle (dotted) line is the susceptibility that generated the signals

for positive, as expected. The ratio of the area of the positive Q-meter output signal to the negative Q-meter output signal is 0.975.

# 4.3. The False Asymmetry of Deuteron TE Signals

The double peaks of the deuteron (spin I=1) spectrum correspond to two quadrupole broadened transitions which partly overlap. If we define  $I_+$  to be the intensity of  $m=1 \leftrightarrow m=0$  transition and  $I_-$  to be the intensity of  $m=0 \leftrightarrow m=-1$  transition, where  $m\equiv \langle I_z\rangle$ , then the two deuteron peaks correspond to the  $I_+$  and the  $I_-$  transitions. Defining the ratio of the intensities of these transitions as  $R=I_+/I_-$  the deuteron polarization can be written in the well-known form

$$P_D = \frac{R^2 - 1}{R^2 + R + 1} \,. \tag{22}$$

Let us calculate the false asymmetry of the deuteron thermal equilibrium (TE) Q-meter calibration signal caused by the frequency dependent coefficient  $G^2(\omega)/\omega$ . According to the Maxwell — Boltzmann distribution, the natural polarization in 2.5 T field and at a temperature of T=1 K, given by the Brillouin function (I=1) as

$$P_D = \frac{4 \tanh (\hbar \omega_D / 2kT)}{3 + \tanh^2 (\hbar \omega_D / 2kT)} = 0.00052,$$
 (23)

where  $\hbar$  is Plank's constant divided by  $2\pi$ , k is Boltzmann's constant and  $\omega_D = 2\pi \times 16.35$  MHz is the deuteron Larmor frequency for a magnetic field of 2.5 Tesla. For the TE polarization, the natural asymmetry of the deuteron signal is found from Eq.(22) as  $R_{\rm nat} = 1.00078$  when  $P_D = 0.052\%$  from Eq.(23).

In order to estimate the false asymmetry we ignore the integral in Eq. (8) and assume that  $r=\alpha=0$ ,  $r_{\rm eff}\equiv |Z_L(\omega_0)|=R=9\Omega$ ,  $p=0.02\Omega^{-1}$ ,  $\omega L\approx \rho=50~\Omega$  so that we have from Eq. (17)

$$\xi_{\pm 0}^{"} \equiv \xi_{\cdot}^{"}(\omega_{:\pm 0}) \approx (1 + 2pr_{\text{eff}}) \left(1 - 2\pi \frac{\Delta \omega_{\pm 0}}{\omega_{0}}\right) \left(\frac{R_{G}}{\omega L}\right) \operatorname{Re}\left(\frac{\Delta V_{\text{out}}(\omega)}{V_{n}}\right) \approx$$

$$\approx 20 \left(1 - 2\pi \frac{\Delta \omega_{\pm 0}}{\omega_{0}}\right) S_{\pm 0}, \tag{24}$$

where  $\Delta\omega_0=0$  and  $\Delta\omega_\pm\equiv\omega_\pm-\omega_0=\pm2\pi\times60$  kHz is the half distance between the peaks of the NMR signal for deuterated 1-butanol d-10. Using an expression for the deuteron asymmetry from [11], we can compare the natural asymmetry to the experimentally measured asymmetry. The natural asymmetry  $R_{\rm nat}=1.00078$  from Eqs. (22, 23), according to [11] must correspond to the peak susceptibility asymmetry

$$R_{\text{nat}} = \frac{\xi_{+}^{"}/\xi_{0}^{"} - 0,707}{\xi_{-}^{"}/\xi_{0}^{"} - 0.707} = 1.00078.$$
 (25)

To calculate the false asymmetry, we have to replace the values of susceptibility in Eq. (25) with the corresponding signal values, which should be calculated from Eq. (24). Thus,

$$R_{\rm exp} = \frac{S_{+}/S_{0} - 0.707}{S_{-}/S_{0} - 0.707} = 1.075.$$
 (26)

The signs (+,-,0) in Eqs. (25,26) are defined in [11] as the signal extrema for the respective  $I_+$  and  $I_-$  transitions, and middle point of the deuteron signal respectively, and  $S_{\pm 0}$  refers to the value of the real part of the signal at those points. From the deuteron experimental TE signals [12] we estimated the ratio  $\xi_+''/\xi_0''\approx \xi_-''/\xi_0''=1.95\pm0.05$  to calculate  $S_\pm/S_0$  from Eq. (24) and  $R_{\rm exp}$  using Eq. (26).

According to Eqs. (22, 26), the polarization is equal to 4.8% at  $R_{\rm exp} = 1.075$  due to the false asymmetry instead of 0.052% which is found by using the asymmetry value  $R_{\rm nat} = 1.00078$ . The above example can be used to illustrate the difficulty in using Eq. (22) inversely to determine  $P_D$  from  $R_{\rm exp}$ . We believe this effect explains the systematic difference between the values of polarization measured by the asymmetry method and the TE method. As a minimum requirement when analyzing enhanced deuteron signals, Eq. (24) must be used as a simple yet necessary correction to the false asymmetry.

# 4.4. The Distortions of NMR Signals Caused by Phase

Eq. (14) enables us to calculate the complex magnetic susceptibility from the NMR signal  $S(\omega) + iT(\omega)$ . However, the Q-meter output voltage, acting on the PSD input, incorporates the complex factor  $V_n = A(\omega)V_C$  (see Eq. (8)).

$$\Delta V_{\text{out}} = A(\omega) V_G \{ S(\omega) + iT(\omega) \}, \tag{27}$$

which must be taken into account for accurate measurements. We define the phase of the rf generator voltage to be zero. With this convention, the complex amplitude  $A(\omega)V_G$  from Eq. (27) is

$$A(\omega)V_G = |A(\omega)V_G| e^{-i\Phi(\omega)}, \tag{28}$$

where  $\Phi(\omega)$  is the phase shift of the amplifier, see Fig.1. The PSD output voltage is equal to

$$\Delta V_{\text{PSD}}(\omega) = |A(\omega)V_G| \{S(\omega) + iT(\omega)\} e^{-i[\Phi(\omega) - \phi(\omega)]}, \quad (29)$$

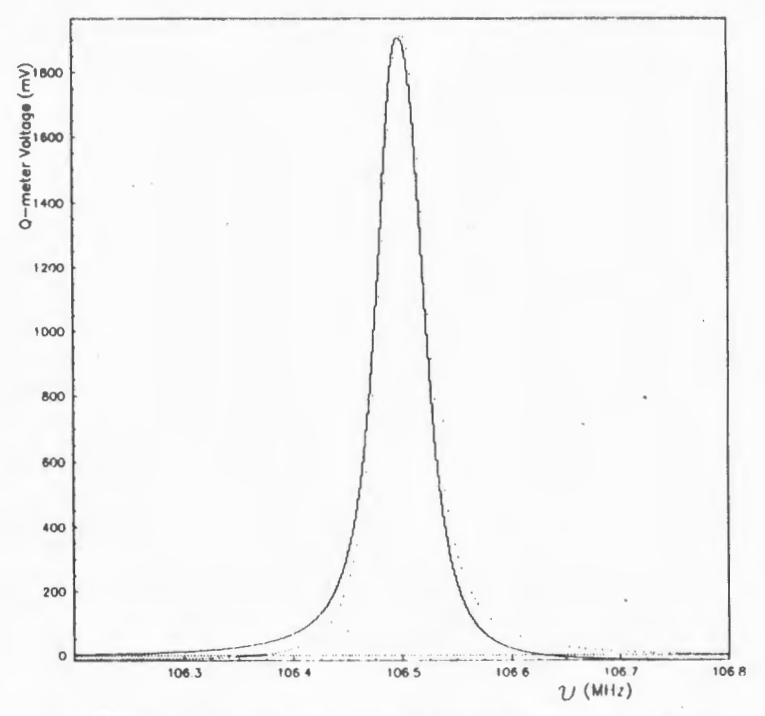


Fig.5. A plot of the distortion of proton signals due to phase shifts. For a symmetric absorption, the Q-meter output voltage is distorted when the phase  $\Phi$  is non-zero. This plot corresponds to a constant phase of  $+5.0^{\circ}$  for the dotted line and a constant phase of  $-5.0^{\circ}$  for the solid line

where  $\phi(\omega)$  is the phase of the voltage applied to the local oscillator (LO) input. We remind that the PSD output voltage does not depend on the amplitude of the LO voltage. It is usually assumed that the phase shift  $\Phi(\omega)$  of the amplifier in the difference  $\Phi(\omega) - \phi(\omega)$  is compensated approximately by using a similar amplifier at the reference input of the PSD (omitted in Fig.1). During the tuning procedure, in accord with Eq. (29) the phase difference  $\Phi(\omega) - \phi(\omega)$  has to be accurately adjusted to zero at the frequency  $\omega_0 = 2\pi\nu_0$ , which is where  $T(\xi=0,\omega_0)=0$  and  $\mathrm{Im}\ \{Z(\xi=0,\omega_0)\}=0$  in Eq. (29). This is so that the PSD detects only the real part of the Q-meter output voltage

$$\operatorname{Re}\left(\Delta V_{\mathrm{PSD}}(\omega)\right) = \left|A(\omega)V_{G}\right| \, S(\omega), \tag{30}$$

which converted to zero intermediate frequency voltage in the PSD. In the absence of the imaginary part of this voltage, the phase tuning of the Q-meter

may be done only approximately using the characteristic Q-curve shape. The error in the setting of the phase relation of PSD gives rise to additional distortion of the signal. It is evident from the plots in Fig.5 showing the proton signal for the phase errors of +5 and -5 degrees. Comparing with plots of Fig.4, which were calculated with  $\phi=0$ , we see the substantial distortion, predominantly in the antisymmetric features appearing in the signal wings. Due to this the integral in Eq.(2) may deviate form the original value by an amount which depends strongly on the zero line position (see Section 6). The Q-meter with detection of the real and imaginary parts will allow more accurate phase tuning in additional to the extraction of the true susceptibitly, using Eq.(14), including the phase correction function  $\Phi(\omega) - \phi(\omega)$  in Eq.(29).

## 5. The Shape of the Q-curve

An accurate TE-calibration normally requires a special experimental procedure (such as immersion in superfluid helium-4) to maintain the sample material at a homogeneous and accurately known temperature where the polarization is described by the Brillouin function. This calibration then remains valid for some period of time during which the polarization is determined by comparison of the integrated signals to the TE signals. After the calibration, we have to estimate and correct in some way the influence of circuit parameter drift on the measurement of target polarization.

Another problem arises with the TE-calibration of small signals such as those of the deuteron. Circuit parameter drift leaves a residual Q-curve, the differential Q-curve (due to temperature drift) superimposing with the TE signal, whose integral can be greater than that of the TE signal. In this case, the TE-calibration is dependent on the procedure used to subtract the Q-curve. Consequently, we would like to know the true equation for the residual Q-curve.

Both problems are addressed by fitting Eqs. (3,4) with  $\xi = 0$  to the measured Q-curves, thus determining the circuit parameters and the residual Q-curve.

The Q-curve is calculated from the real part of Eq. (3) with  $\xi = 0$ . Separating the real and imaginary parts of Eq. (3) gives [3]

$$\operatorname{Re}\left\{\frac{V_{\text{out}}(\omega)}{V_{n}}\right\} = \frac{1}{R_{G}} \left\{\frac{\operatorname{Re}(Z) + p\{\operatorname{Re}^{2}(Z) + \operatorname{Im}^{2}(Z)\}}{[1 + p\operatorname{Re}(Z)]^{2} + p^{2}\operatorname{Im}^{2}(Z)}\right\}$$
(31)

and

$$\operatorname{Im}\left\{\frac{V_{\text{out}}(\omega)}{V_n}\right\} = \frac{1}{R_G} \left\{\frac{\operatorname{Im}(Z)}{\left[1 + p\operatorname{Re}(Z)\right]^2 + p^2\operatorname{Im}^2(Z)}\right\}. \tag{32}$$

The real part can be rewritten in the form

$$\operatorname{Re}\left\{\frac{V_{\text{out}}(\omega)}{V_n}\right\} = \frac{1}{pR_G} \left\{ 1 - \frac{1 + p\operatorname{Re}(Z)}{\left[1 + p\operatorname{Re}(Z)\right]^2 + p^2\operatorname{Im}^2(Z)} \right\}$$
(33)

Then using relations taken from [1] and applying them to Eq.(4) we find [6]

$$\operatorname{Re}\left\{\frac{V_{\operatorname{out}}(\omega)}{V_n}\right\} =$$

$$= \frac{1}{pR_G} \left\{ 1 - \frac{1 + p(R + A_1/A_0)}{\left[1 + p(R + A_1/A_0)\right]^2 + p^2 \left[A_2/A_0 - 1/\omega C_p\right]^2} \right\}, \tag{34}$$

where

$$A_0 = 1 - 2k_2 \frac{\omega L}{\rho} + 2k_1 \frac{r}{\rho} + (k_1^2 + k_2^2) \left\{ \left( \frac{r}{\rho} \right)^2 + \left( \frac{\omega L}{\rho} \right)^2 \right\}, \tag{35}$$

$$A_1 = r \left\{ 1 + k_1 \frac{r}{\rho} + (k_1^2 + k_2^2) \right\} + \rho k_1 \left\{ 1 + \left( \frac{\omega L}{\rho} \right)^2 \right\}$$
 (36)

and

$$A_2 = \omega L \left\{ 1 - (k_1^2 + k_2^2) \right\} + \rho k_2 \left\{ 1 - \left( \frac{r}{\rho} \right)^2 - \left( \frac{\omega L}{\rho} \right)^2 \right\}. \tag{37}$$

We have made use of the relation  $tanh(\gamma l) = k_1 + \iota k_2$ , where

$$k_1 = \frac{\tanh(\alpha l)}{k_3 \cos^2(\beta l)}, \quad k_2 = \frac{\tan(\beta l)}{k_3 \cosh^2(\alpha l)}, \quad k_3 = 1 + \tanh^2(\alpha l) \tan^2(\beta l).$$
 (38)

It is clear from Eq. (34) that the resonance value for the capacitance is very close to  $C_p = A_0/A_2/\omega$  so this formula can be used for either a hybrid or normal resonance circuit.

Using this method, a baseline fit can be made at any time in order to calculate new values for the drifting circuit parameters. These new values can then be used in Eq.(14) to correct the NMR signals, thus producing a method to compensate for parameter drift in the time between measuring the TE-calibration signals.

Let us determine as an example the drift in the baseline during the TE-calibration due to the temperature drift of  $\gamma L$ , we take the derivative with respect to  $\gamma L$  of Eq. (3) at  $\xi = 0$  which gives

$$\frac{V_{\text{out}}(b\gamma(t)) - V_{\text{out}}(b\gamma(t=0))}{V_n} = \left[\frac{\rho^2 - (r + \iota \omega L)^2}{\rho R_G G^2(\omega)}\right] \{b\gamma(t) - b\gamma(t=0)\}, \quad (39)$$

where  $\gamma(t=0)$  is the value of the complex propagation constant at the start of the TE-calibration and  $\gamma(t)$  is its value a time t later. These values are determined by fitting Eq. (34) to the baseline signal.

#### 6. Errors in the Polarization Calculation

Within the scope of the series Q-meter, it is useful to mention some important considerations in the calculation of the polarization. As is well known, the absorption part of the susceptibility describes the frequency distribution of the spins near the NMR Larmor frequency, and its integral is proportional to the nuclear polarization. Strictly speaking, the polarization is

$$P = C \int_{0}^{\infty} \xi'(\omega) d\omega.$$
 (40)

However, in practice the absorption can only be measured in a small range around the Larmor frequency. Thus, the integral in Eq.(40) is measured over restricted limits. Moreover, it is generally assumed that the Q-meter signal,  $S(\omega)$ , is proportional to  $\xi''(\omega)$  and that

$$P = C_s \int_0^\infty S(\omega) d\omega, \tag{41}$$

where the constant of proportionality,  $C_s$  is a function of the modulation, the circuit parameters, and the target material. But, the general theory of linear two terminals [7] tells us that the integral in Eq. (41) can be calculated independent of the circuit parameters as

$$\int_{0}^{\infty} \{S(\omega) - S_{\infty}\} d\omega = -\frac{\pi}{2} \lim_{\omega \to \infty} \omega T(\omega), \tag{42}$$

where  $S(\omega)$  and  $T(\omega)$  were described in Eq.(8) and

$$S_{\infty} = \lim_{\omega \to \infty} S(\omega). \tag{43}$$

Typically the wings of an absorption line fall down faster than for a Lorentzian function. For a Lorentzian shape, the absorption and dispersion will fall off asymptotically at least as fast  $\omega^{-2}$  and  $\omega^{-1}$  respectively. Multiplying

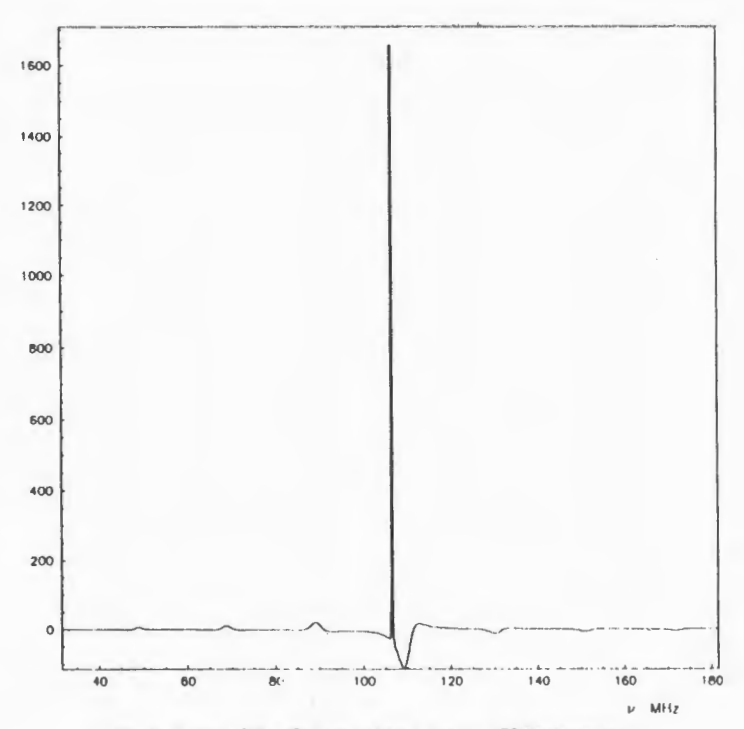


Fig. 6. A plot of the Q-meter signal over a 150 MHz sweep

Eq. (13) by  $\omega$  and taking the limit  $\omega \to \infty$ , we see that the numerator goes like  $\omega$  and the denominator like  $\omega^2$ , so the quantity  $\omega \Delta V_{\text{out}}(\omega)/V_n$  falls off like

$$\omega^{-1}$$
. The result is that 
$$\int_{0}^{\infty} S(\omega) = 0$$
 (44)

such that the integral is not dependent on the receiving circuit's parameters. The function  $S'(\omega)$  is plotted in Fig.6 for a very wide sweep. The effect of the cable and slowly decaying dispersion tail on the circuit inductance is visible. In this figure, the cable nodes occur every 21.3 MHz, which is what is expected for a cable with length  $5\lambda/2$  at 106.5 MHz Larmor frequency.

The shape of the signal must be taken into account when designing the Q-meter and when calculating the errors in the polarization measurement. In fact, one can see from Figs.3 and 5 that signal crosses the zero line on both sides of the Larmor frequency. This produces an extra error depending on where one draws the line about which  $S(\omega)$  is integrated. That is, the signal voltage should be allowed to cross zero when calculating the integral,

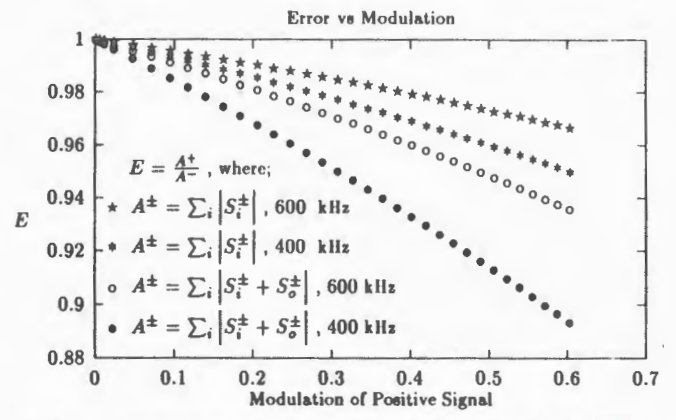


Fig. 7. An illustration of error in the proton polarization measurement shown as a function of modulation M for positive polarization. The measure of error is the ratio of the positive signal's integral to the negative signal's integral for susceptibilities differing only in sign. The constant  $S_0(\omega)$  is an offset added so that each signal has the same sign over the entire frequency sweep (i.e., the signal wings do not cross zero)

and should not be offset such that it always has the same sign. There is a difference of a factor of two in the error for the two cases. This is plotted in Fig.7.

#### 7. Conclusions

We have presented a new Q-meter theory for accurate measurements of nuclear polarization. From this analysis it is clear that new techniques must be developed based on the principles embodied in Eqs. (14,34) of this paper because the usual methods, based on series expansions of Eqs. (3,4), cannot be easily adapted to correct experimental data. We list the next steps in the development of polarization measurements:

1. The series Q-meter [5] needs to be improved by the addition of a separate phase sensitive detector to measure the imaginary part as well as the real part of the Q-meter output signal. Also, one ought to add a function converter (see Fig.1) which calculates  $\xi(\omega)$  from  $\Delta V_{\text{out}}(\omega)$  via Eq.(14). It is  $\xi(\omega)$ , not  $\Delta V_{\text{out}}(\omega)$ , whose integral is exactly proportional to the nuclear polarization. The reason for measuring the imaginary part of the Q-meter signal is to avoid the numerical calculation of the integral in Eq.(8), thus allowing fast and accurate corrections due to dispersion effects.

- 2. The crigins of the false asymmetry of the deuteron signal and the distortions of the proton signal are demonstrated and henceforth can be accounted for.
- 3. It is proposed to determine circuit parameters by fitting Eq. (34) to data. This would allow a method for accurate correction of the polarization for circuit parameter drift during long periods between TE calibrations.
- 4. The experimental calibration signals can be corrected for the residual Q-curve by fitting Eq. (39) to real data. This residual contribution is caused by temperature drift of circuit elements such as the complex propagation constant  $\gamma$  during long time it takes to gain high statistics for the TE-signals.
- 5. The susceptibility now be corrected for errors caused by the dependence of the phase on the frequency. Within the scope of this theory, the effects of phase distortions can now be accounted for for the first time.

# Acknowledgements

This work has been made within the Spin Muon Collaboration (SMC) at CERN. We would like to thank C.Whitten, F.Lehar and D.Pose for useful remarks. Y.K. is grateful to V.Hughes, G.Mallot, R.Voss for support. This work was partially supported by the US Department of Energy, the Laboratory of Particle Physics (JINR) and the SMC.

We wish to thank Yannis Semertzidis for helpful discussions, many of which led to corrections in the numerical calculations performed in this work.

## References

- 1. Petricek V. Nucl. Instr. and Meth., 1968, 58, p.111.
- 2. Ryter C. Nucl. Instr. and Meth., 1967, 49, p.267.
- 3. Niinikoski T.O. In: Proc. of the 2nd Int. Workshop on Polarized Target Materials, G.R.Court, D.A.Cragg and T.O.Niinikoski (eds.), report RL-80-080, SRC, Rutherford Laboratory, 1980, p.80.
- 4. Gifford D. In: Proc. of the 2nd Int. Workshop on Polarized Target Materials, G.R.Court, D.A.Cragg and T.O.Niinikoski (eds.), report RL-80-080, SRC, Rutherford Laboratory, 1980, p.85.
- 5. Court G.R., Gifford D.W., Harrison P., Heyes W.G., Houlden M.A. Nucl. Instr. and Meth., 1993, A324, p.433.
- Kisselev Yu.F. The Theory of Q-Meter, Geneva, CERN, SMC note, 1993, 20
- 7. Bode Hendrik W. Network Analysis and Feedback Amplifier Design, New York: Van Nostvard, 1945 (repr. 1953), p.563.

- 8. Abragam A. The Principles of Nuclear Magnetism, Clarendon Press, Oxford, p.93.
- 9. Hill John J., Hill Daniel A. Nucl. Instr. and Meth., 1974, 116, p.269.
- 10. Sperisen F. Nucl. Instr. and Meth., 1987, A260, p.455.
- 11. Kisselev Yu.F., Popov S.A., Fedorov A.N. Pis'ma Zh. Eksp. Teor. Fiz., January 25, 1992, 55, No.2, p.99.
- Magnon A. and Polarized Target Group, CERN (PPE) Saclay, SMC note, 1992, 15, p.24.

# AN EXPERIMENTAL RUN ON THE NEW SUPERCONDUCTING ACCELERATOR NUCLOTRON AT 3.8 AND 6.2 GeV/c DEUTERON MOMENTUM

A.M.Baldin, Kh.U.Abraamyan, S.V.Afanasiev, Yu.S.Anisimov, V.V.Arkhipov, A.S.Artyomov, V.V.Avdeichikov, V.K.Bondarev, A.F.Elishev, A.Yu.Isupov, V.A.Kashirin, A.N.Khrenov, V.I.Kolesnikov, A.D.Kovalenko, V.A.Kuznetsov, A.G.Litvinenko, A.I.Malakhov, P.K.Maniakov, E.A.Matyushevsky, G.L.Melkumov, I.I.Migulina, A.S.Nikiforov, V.A.Nikitin, P.V.Nomokonov, V.G.Perevozchikov, S.G.Reznikov, J.A.Rufanov, A.Yu.Semenov, V.A.Smirnov, P.I.Zarubin, I.Atanasov<sup>1</sup>, V.IN.Penev<sup>1</sup>, A.I.Berlev<sup>2</sup>, V.A.Krasnov<sup>2</sup>, A.I.Maevskaia<sup>2</sup>, S.V.Zadorozny<sup>2</sup>

The new superconducting accelerator Nuclotron has been operated for the first time at 3.8 and 6.2 GeV/c deuteron momentum and the run on the internal target has been carried out in March'94. The measurements were done in the framework of SPHERE, SYaO and DELTA (INR, Treitsk) projects. There were used various scintillation counters for  $\Delta$  E-E and time-of-flight (TOF) measurements, the silicon and CsI crystal detectors for  $\Delta$  E-E measurements as well, and the lead glass EM calorimeters. The secondary particles  $\gamma$ ,  $\pi$ , K, p, d, and t as well as He fragments produced by deuterons on the internal targets were detected and identified reliably, thus manifesting a broad perspective of the relativistic nuclear physics research on Nuclotron in the nearest future.

The investigation has been performed at the Laboratory of High Energies, JINR.

Экспєримент на новом сверхпроводящем ускорителе Нуклотрон при импульсе дейтронов 3,8 и 6,2 ГэВ/с

А.М.Бал,дин и др.

На новом сверхпроводящем ускорителе Нуклотрон в марте 1994 года впервые ускорены дейтроны с импульсами 3,8 и 6,2 ГэВ/с и выполнены измерения с использованием внутренних мишеней. Работа осуществлена в рамках проектов СФЕРА, СЯО и ДЕЛЬТА (ИЯИ, Троицк). Были использованы различные сцинтилляционные детекторы для измерения  $\Delta E - E$  и премени пролета частиц, кремневые детекторы и детекторы на основе кри сталлов CsI, также для измерения  $\Delta E - E$ , и электромагнитные

<sup>&</sup>lt;sup>1</sup>Institute or Nuclear Research and Nuclear Energy, Sofia, Bulgaria

<sup>&</sup>lt;sup>2</sup>Institute or Nuclear Research of the Russian Academy of Sciences, Moscow, Russia

калориметры из свинцового стекла. Зарегистрированы и надежно идентифицированы вторичные частицы  $\gamma$ ,  $\pi$ , K, p, d и t, а также Не фрагменты, рожденные дейтронами на внутренних мишенях, демонстрируя тем самым широкую перспективу для исследования релятивистской ядерной физики на Нуклотроне в ближайшем будущем.

Работа выполнена в Лаборатории высоких энергий ОИЯИ.

A specialized superconducting strong-focusing accelerator of nuclei Nuclotron [1] is proposed, constructed and commissioned at the Laboratory of High Energies of the Joint Institute for Nuclear Research in order to continue a wide programme of relativistic nuclear physics started in 1971 at Dubna Synchrophasotron [2]. The main research goals are the study of the quark-gluon degrees of freedom in nuclei and the excited nuclear matters [3].

The Nuclotron beams can be used for studying practically all characteristics of highly excited nuclear matter including the asymptotic value estimated roughly as 3.5 GeV/c per nucleon for projectile nucleus momentum. This value was obtained from the universal approch [4] to the analysis of multiparticle production processes based on the relativistic invariant quantities  $b_{ik} = -(p_i/m_i - p_k/m_k)^2$  in four-dimensional velocity space of particles involved in the reaction, as well as from the experiments

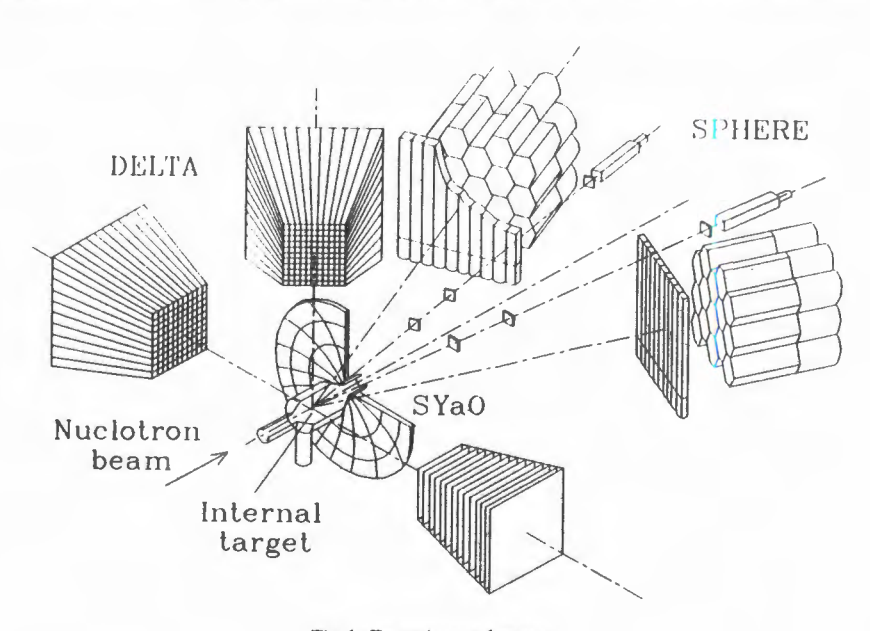


Fig.1. Experimental setup

on the inclusive pion production [5,6]. The experiments on the Nuclotron internal beams make it possible to study a large variety of nucleus-nucleus collisions with changing continuously the kinetic energy of incident nucleus, thus to research «the transition regime» from nucleon to quark-qluon matter grounding QXD primarily.

We announced already on successful operation of Nuclotron and the first experiments on deuterons at 200 MeV/nucleon kinetic energy in July

1993 [7].

This report is dedicated to the measurements carried out on the Nuclotron using the internal targets at deuteron momentum of  $3.8~{\rm GeV/c}$  in March 1994. Moreover, it was succeeded at the end of the run to accelerate deuterons up to  $6.2~{\rm GeV/c}$  momentum for short running period, thus to reach the half maximum of the energy designed for Nuclotron.

Three experimental groups SPHERE, SYaO and DELTA (INR, Troitsk) have been joined in performing the measurements on the Nuclotron using the internal targets.

The schematic diagram of the present and future status of the experimental setup is shown in fig. 1. The setup includes:

SPHERE: multichannel lead glass EM calorimeter,

 $\Delta E-E$  and TOF scintillation counters.

SYaO:  $\Delta E - E$  telescopes of silicon detectors and

CsI or BGO crystals, and plastic scintillators.

DELTA: high granularity lead glass EM calorimeter,

multiplate  $\Delta$  E-E and TOF scintillation counters.

The experimental facility involves also the internal target operation equipment and the system to control the intensity and the lifetime of the beam interacting with the target operated inside the accelerator vacuum tude [8]. The principle of the beam control is based on detection of the target material radiation by means of the photomultiplier and tandem-microchannel-plate detector in vacuum. The corresponding time structure of the beam interaction with target foils as well as its fine structure are presented in fig.2a and fig.2b, respectively.

General information on the run is:

Beam deuterons.

Momentum: 3.8 GeV/c at B = 0.6 Tesla,

6.2 GeV/c at B = 1.0 Tesla.

Beam intensity:  $\sim 10^9/\text{spill}$ . Beam duration:  $\sim 300 \text{ ms}$ .

Target foils:  $1.57 \mu \text{km CH}_2$  and  $1.72 \mu \text{km Au}$ .

Exposition of detectors:  $\sim 8$  hours. Triggers:  $\sim 10^5$ /detector.

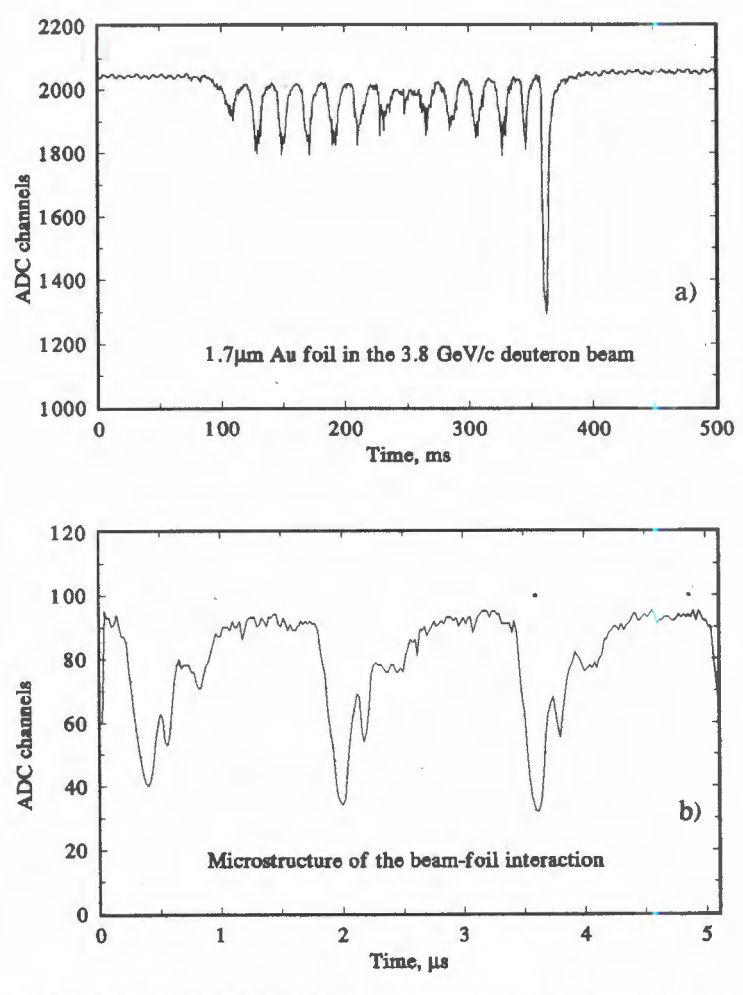


Fig. 2. a) Time structure of the beam-target interaction. b) Time microstructure of the beam-target interaction

The following detectors operated at the present run:

— Two identical telescopes containing four scintillation counters each with  $2\times2\times0.5$  cm<sup>3</sup>,  $3\times3\times0.5$  cm<sup>3</sup>,  $4\times4\times0.5$  cm<sup>3</sup> and  $7.5\times7.5\times65$  cm<sup>3</sup>, respectively. The first three counters are aimed for  $\Delta E$  and TOF measurements, and the last one for the measurement of charge particle energy E. The on-line scatter plot of TOF vs energy loss on fig.3a demonstrates qualitatively the  $\pi$ , p, d, t, and He separation capability.

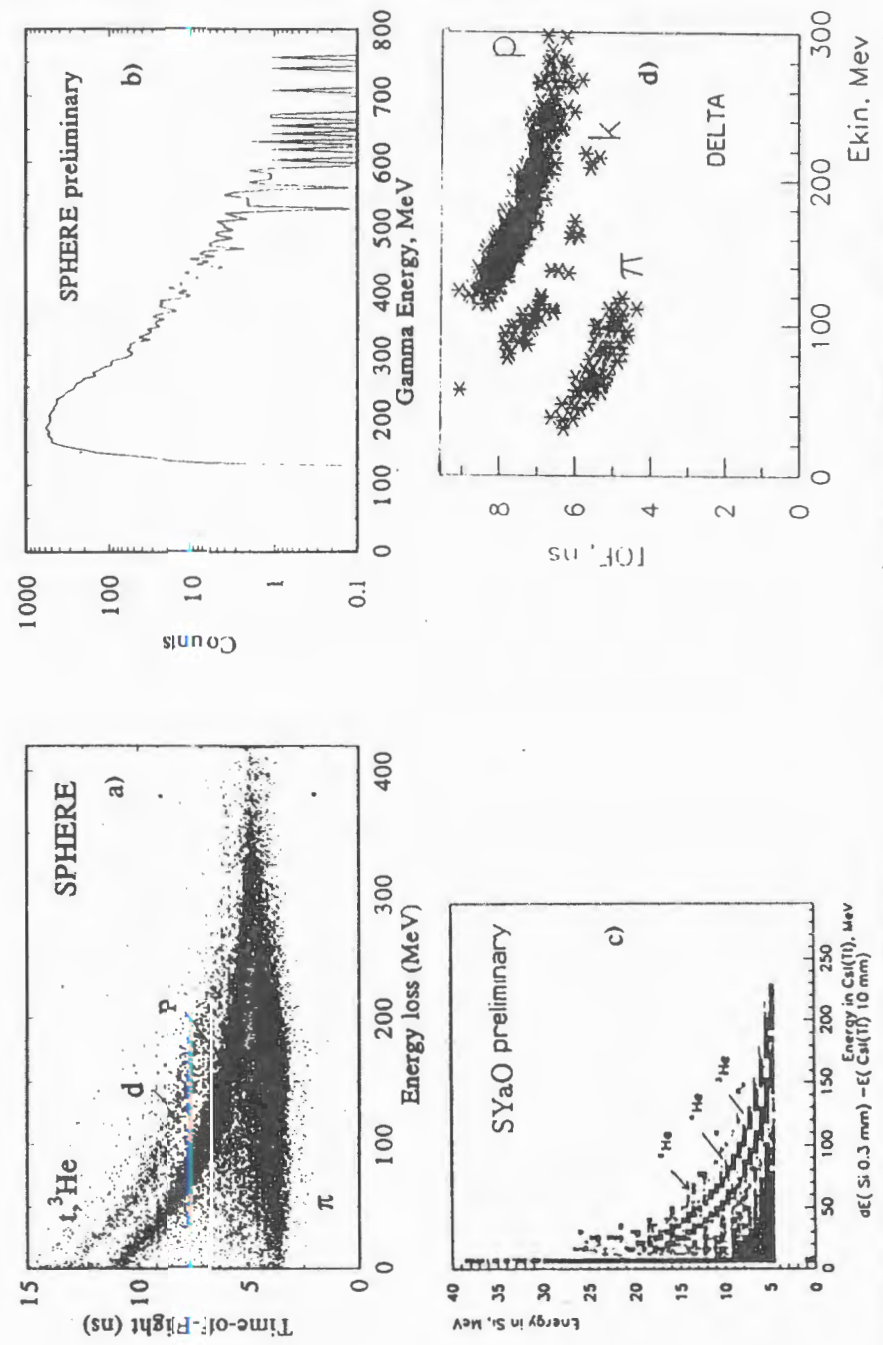


Fig.3. March'94 Nuclotron run on the internal target d + Au + ... at  $P_d = 3.8$  GeV/c: a) scatter plot TOF vs energy loss for secondary  $\pi, p, d, t$ , and He, b) lead glass calorimeter spectrum for  $\gamma$ -quanta, c)  $\Delta E - E$  scatter plot for secondary He fragments, d) TOF vs  $E_{kin}$  scatter plot for  $\pi$ , K and p. Kaons are subthreshold ones

- Two arms of 36 lead glass EM calorimeter modules are located behind 1m×1m scintillation hodoscopes. Each module radiator 35 cm (14 r.l.) long is hexagonal in form with 17.5 cm inscribed circle diameter. The one-line spectrum of gamma-quanta detected by EM calorimeter is shown in fig.3b and it looks rather reasonable for having no visible overlaps of two particle hits.
- Telescope is assembled of Si (0.3 mm) transmission detector and CsI(Tl) (10 mm) crystal for  $\Delta E$  and E measurements of the nuclear fragments, respectively, as it's already evidenced on the sample of  $^3\text{He}$ ,  $^4\text{He}$  and  $^6\text{He}$  secondaries in fig.3c. CsI(Tl) detector was provided with the silicon photodiode readout.

— Scintillation spectrometer for multiple sampling is assembled of 14 layers of scintillator with dimensions increasing gradually from 16×16×2 cm<sup>3</sup> for the 1st to 27×27×4 cm<sup>3</sup> for the 14th plate. The scintillation TOF detector is placed between the target and this spectrometer. The scatter plot of the charge particle kinetic energy E (MeV) vs TOF (ns) is shown

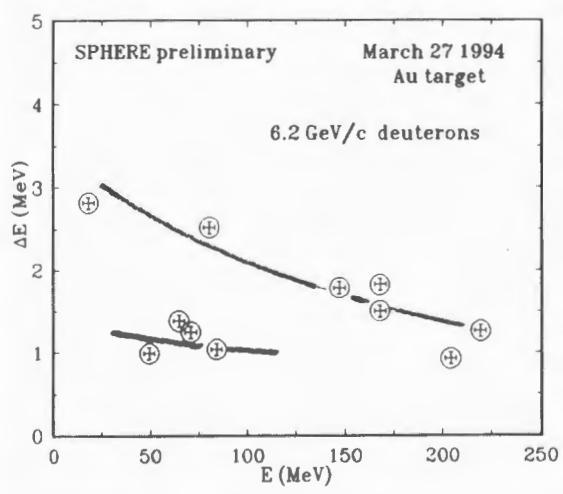


Fig. 4. March'94 Nuclotron run on the interal target  $d+\mathrm{Au} \Rightarrow \dots$  at  $P_d=6.2~\mathrm{GeV/c}$ .  $\Delta E-E$  scatter plot for secondary particles

in fig.3d. Being very preliminary this off-line data show, nevertheless, a clear separation of pions, kaons, and protons. The most remarkable is that all kaons are subthreshold ones.

Finally, we show ΔE
vs E scatter plot (fig.4),
which is unique one
although it contains few
events, as they are the first
pions and proton:s produced
on Nuclotron at deuteron
250 momentum of 6.2 GeV/c.

In conclusion, the main goal of the run was considerable increasing of the accelerated particle energy, thus all detectors and

internal target system operated in tuning regime of accelerator complex. Nevertheless, the above-mentioned data manifest the reliable perspective of relativistic nuclear physics research on Nuclotron in the nearest fluture.

This work has been carried out owing to the great effort and support of the numerous staff of engineers, physicists and technicians at the Laboratory of High Energies (JINR) and we are very much obliged to them for it could not have been done without their assistance.

The experiment was promoted by the Russian Grant for Fundamental Research (93-02-3773).

#### References

- 1. Baldin A.M. et al. IEEE Trans. Nucl. Science, 1983, vol.NS-30, No.4, p.3247.
- 2. Baldin A.M. Kratkije Soobshchenija FIAN, Moskva, 1971, p.35;
  - Proc. Rochester Meeting APS/DPF, 1971, p.131.
  - JINR Preprint P1-5819, Dubna, 1971.
- 3. Baldin A.M., Malakhov A.I. JINR Rapid Commun., No.3[60]-93, Dubna, p.52.
- 4. Baldin A.M. et al. Zeitschrift für Physik, 1987, C33, p.363.
- 5. Baldin A.M. et al. Yadernaja Fizika, 1974, 40, p.1201.
- 6. Shroeder L.S. et al. Phys. Rev. Lett., 1979, 43, p.24.
- 7. Baldin A.M. et al. JINR Rapid Commun., No.4[61]-93, Dubna, p.13.
- 8. Artiomov A.S. JINR Rapid Commun., No.4[61]-93, Dubna, p.6.

# SOME RESULTS OF MCP TIMING RESOLUTION MEASUREMENTS WITH MINIMUM IONIZING PARTICLES

A.A.Baldin<sup>1</sup>, L.G.Efimov, G.A.Feofilov<sup>2</sup>, S.N.Filippov<sup>1</sup>, V.S.Pantuev<sup>1</sup>, F.F.Valiev<sup>2</sup>

First results of the timing resolution tests done with 800 MeV/c pion and proton beams for the MCP-based detector are reported. Two chevron stacks of multichannel plate (MCP) detectors with dimensions 43×63 mm² were used together with the multipad readout anodes. The detectors were placed at 34 mm distance one from another along the beamline inside the vacuum chamber. The value 285 psec (FWHM) was obtained for the TOF spectra both for pions and protons.

The investigation has been performed at the Laboratory of High Energies, JINR.

Некоторые результаты измерений временного разрешения МКП для минимально ионизирующих частиц

# А.А.Балдин и др.

Приводятся первые результаты измерений временного разрешения детектора на основе микроканальных пластин (МКП), полученные на пучках пионов и протонов с импульсом 800 МэВ/с. Использовались две сборки МКП детекторов с размерами 43×63 мм² совместно с многопадовой анодной системой. Детекторы располагались в вакуумной камере на расстоянии 34 мм по пучку. Для времяпролетного спектра получена ширина на полувысоте 285 псек как для пионов, так и для протонов.

Работа выполнена в Лаборатории высоких энергий, ОИЯИ.

#### 1. Introduction

This work is aimed at the experimental investigation of the high timing features of MCP detectors that can be used in a wide range of experiments with MIPs. Results of the previous studies [1] of the efficiency of MCP detectors for the MIPs registration stimulated our proposals for the new type coordinate and time sensitive detectors [2]. Now the work is being carried

<sup>&</sup>lt;sup>1</sup>INR, Institute for Nuclear Research, RAS, Moscow, Russia

<sup>&</sup>lt;sup>2</sup>SPbSU, St. Petersburg State University, St. Petersburg, Russia

out on the design of the MCP Forward Multiplicity Detector of the future ALICE detector at the LHC [3]. Besides being used as charge particle multiplicity counter this MCP detector is supposed to be applied as Z-coordinate primary vertex detector and can be included into the First Trigger. The expected excellent timing characteristics of MCPs [4] were not sufficiently studied previously with minimum ionizing particles.

Below we describe briefly the MCP-based multipad detector prototype designed for the future LHC environment and give the details of timing resolution measurements done for a set of two detectors.

# 2. Detectors and Experimental Setup

Measurements were done at the KASPIY magnetic channel of the INR located at the Laboratory of High Energy, JINR, Dubna. Pions and protons with momentum 800 MeV/c, beam size  $10 \times 10 \text{ cm}^2$  and intensity  $10^2 - 10^3$  per spill were used as well as  $\beta$ -source.

We used rectangular MCPs with conventional parameters: material — (SiO<sub>2</sub>) PbO, density 3.89 g/cm<sup>3</sup>, sensitive area 43×63 mm<sup>2</sup>, thickness

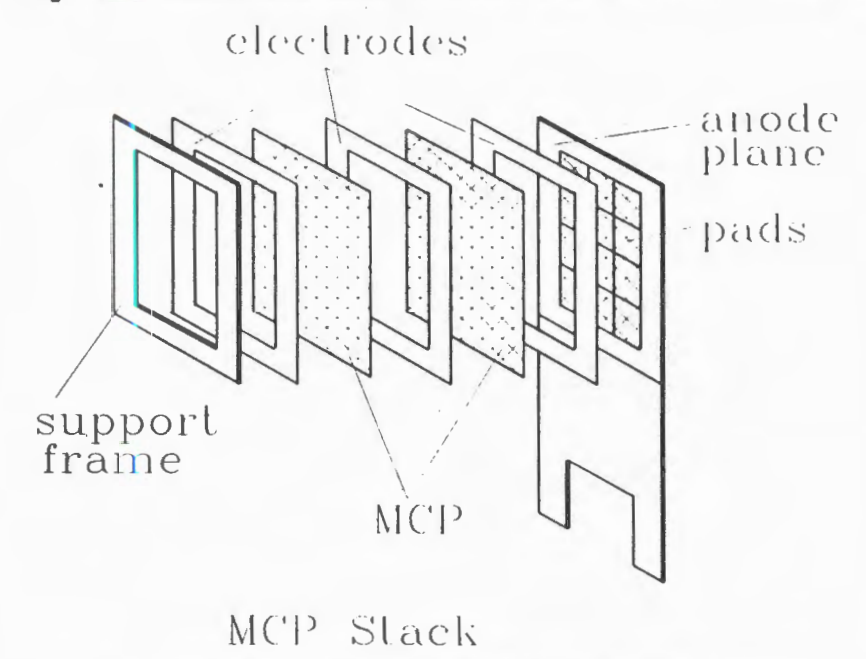


Fig.1. Artistic view of the MCP stack. The transmission lines are positioned on the backplane of the anode plate

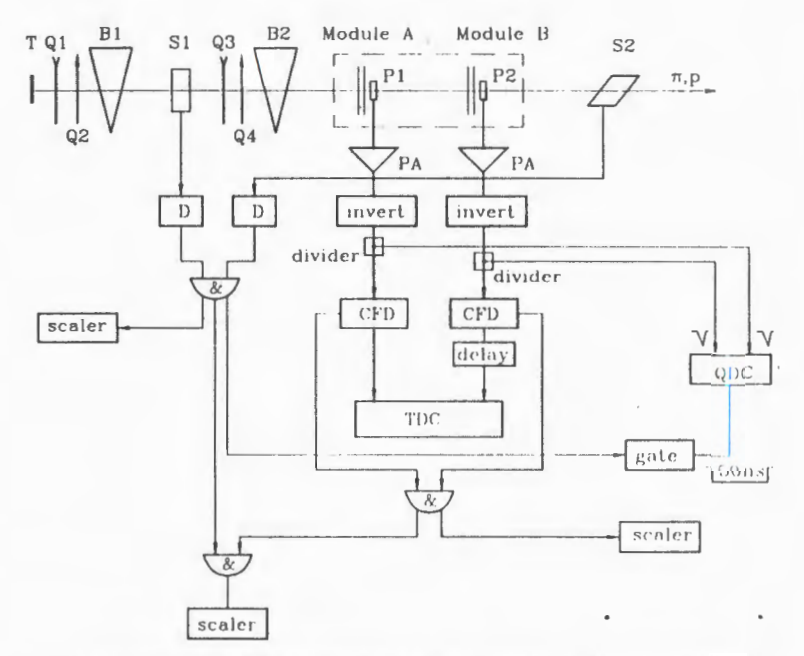


Fig. 2. Schematic view of the channel and the block diagram of the electronics. T—target, Q1-Q3—magnetic lenses, B1-B2—magnetic dipoles, S1-S2—scintillation counters, P1-P2—pads, PA—current preamplifiers, D—discriminators, CFD—constant fraction discriminators, QDC—charge-to-digital converters, TDC—time-to-digital converter

770  $\mu$ m, channel diameter 15  $\mu$ m, channel pitch 17  $\mu$ m, channel bias angle 7°, resistance 6.4·10<sup>8</sup> Ohm, gain 1.6·10<sup>4</sup> at U = 1.14 kV.

The general layout of one MCP-based large area multipad detector is given in Fig.1. It consists of two MCPs mounted in a chevron type stack and a special multipad readout anode combined with 50 Ohm transmission lines [5]. Pads have 13×15 mm<sup>2</sup> size arranged in 3×4 matrix. For technical reasons we have chosen rather large interplate distance 0.5 mm for each stack. The distance between last MCP plate and anode was 0.25 mm.

Two similar modules were mounted on the flange at the distance of 34 mm and placed into the vacuum chamber along the beam line. The vacuum chamber had two mylar  $28 \times 16 \text{cm}^2$  windows of 250 micron thickness. Operating pressure was  $(1+3) \cdot 10^{-6}$  Torr. An external high voltage divider was used for each detector. It supplies equal HV for MCPs in the stack, some potential between MCPs, and a collecting potential about 100 V between the last MCP and the anode.

Signals from the anode pads were enhanced by current preamplifiers with 3 nces rise time (resulted in 5 nsec rise time and 20 nsec duration after 30 meters of cable) and the gain about 40 (or  $2 \text{ mV}/\mu\text{A}$ ).

The block diagram of the electronics used for measurements with beam particles is presented in Fig.2. We used one pad in the first module and one pad in the second one. Signal after preamplifier was splitted to two equal pulses by passive divider. One pulse was sent to QDC, another one after Constant Fraction Discriminator (CFD) was used as start/stop input for TDC and for coincidence measurements. Two identical plastic scintillator counters S1 and S2 having sizes  $10\times10~\text{cm}^2$  were used for QDC gating. S1 was mounted in intermediate focal plane of the magnetic channel 7.2 meters upstream, S2 was positioned just behind the vacuum chamber.

#### 3. Results and Discussion

Operating conditions of the MCP detectors were tested with a collimated  $\beta$ -source prior to measurements with beam particles.

In our case the applied voltage was  $2.5\,\mathrm{kV}$  for the stack or  $1.2\,\mathrm{kV}$  for one MCP plate and was restricted by ion feedback. All presented results were obtained at this voltage. The interplate voltage obtained after some adjustment was  $-100\,\mathrm{V}$ . It cleared the signal and suppressed the positive ion feedback in a wide range of the applied voltage. Nevertheless, as can be seen from Fig.3, where collected charge from one pad is shown, we are far from the saturation mode.

The test measurements of counting rate from  $\beta$ -source and noise versus applied HV are shown in Fig.4. The efficiency of registration of MIPs by this MCP detector was tested with particle beams by usual method of two- and three-fold coincidences between S1, P1 and P2 (See Fig.2). The measured dependence of the efficiency on HV is shown in Fig.5. The geometric factor +25% was taken into account. It reflects an angular spread of particles in the beam about  $\pm$  70 mrad. Estimations of this geometric factor were made with the program code DECAY TURTLE. Within the errors we did not find the efficiency plateau: it grows steadily with HV reaching the value more than 80% at the maximum. This value is close to that from [1] and may be explained by the rather high CFD threshold and hence by some amount of amplitudes under the threshold.

The result of the timing resolution measurement is presented in Fig.6. Signals from two MCP detectors were used as start-stop inputs for TDC. The TDC channel width is  $95 \pm 5$  psec. The timing resolution (for two detectors and electronics) is 3 TDC's channels that corresponds to FWHM = 285 psec.

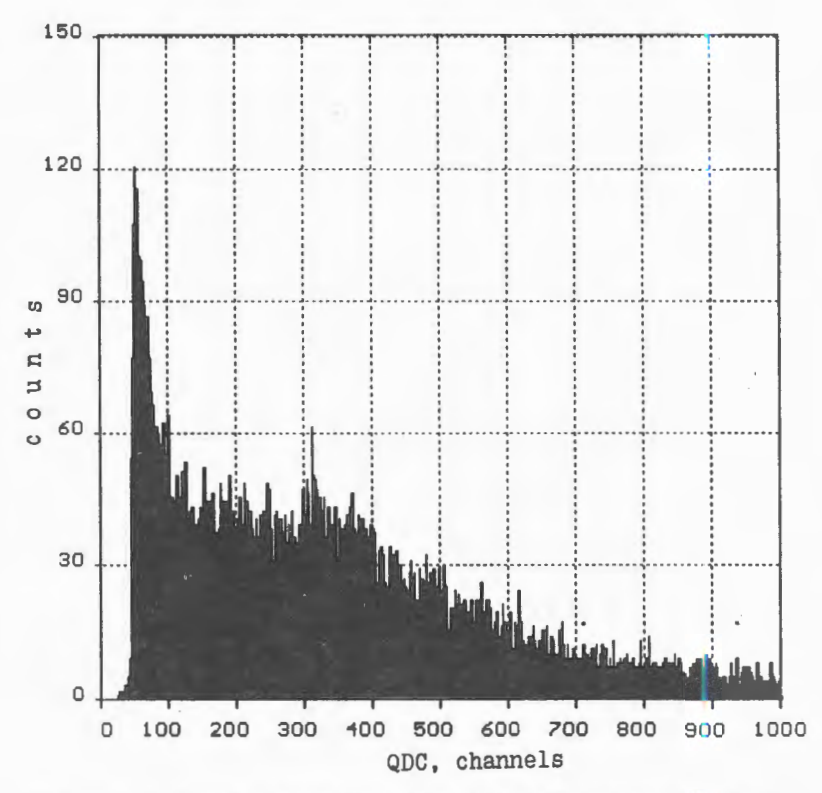


Fig. 3. The pulse height spectrum from one pad of the MCP detector obtained with  $\beta$ -source

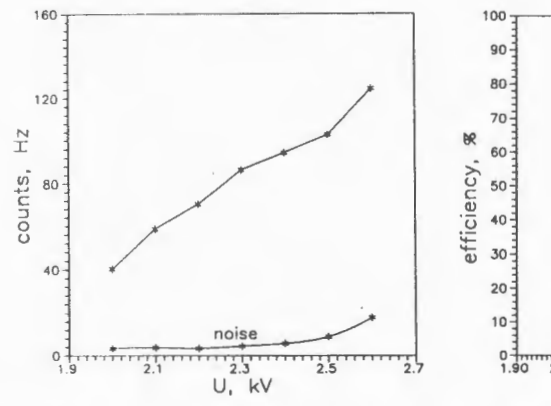


Fig. 4. The counting and noise rates for one pad measured with  $\beta$ -source

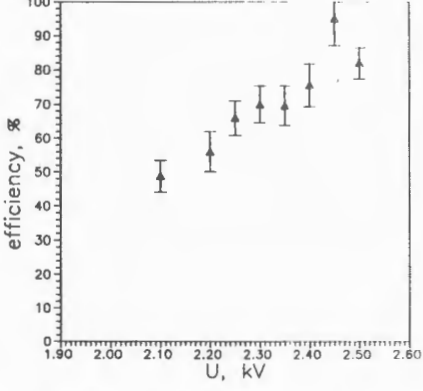


Fig. 5. The efficiency vs. HV for one pad measured with pions and protons at 800 MeV/c  $\,$ 

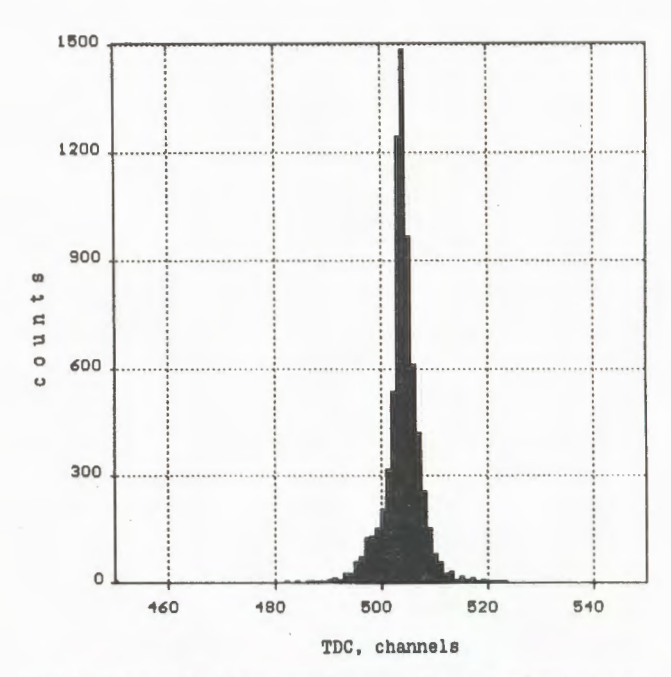


Fig.6. Time-of-flight spectrum for two pads measured with pion and proton beam at 800 MeV/c. The distance between pads is 34 mm. FWHM is 285 psec. The TDC channel width is 95  $\pm$  5 psec

#### 4. Conclusions

First results of the timing resolution tests at 800 MeV/c pion and proton beams for two MCP-based multipad detectors are reported. Two chevron stack of  $43\times63 \text{ mm}^2$  sensitive area MCPs were used together with the multipad readout anodes. The value FWHM = 285 psec was obtained for the TOF spectra both for pions and protons.

In order to improve further the timing resolution it is necessary to optimize the geometry of the detectors and exploit MCPs in saturation mode. The later is preferable for using MCP as a multiplicity detector [3] due to better signal to noise ratio and peaked signal electron pulse height attainable for this regime.

It would be useful also to test these detectors at lower pressure of ambient gas close to that of LHC, where the effect of ion feedback is negligible.

## 5. Acknowledgments

We would like to express sincere gratitude to a lot of people from JINR who helped us in the preparations of this work: to the engineering staff of the synchrophasotron for the possibility of our investigations with high quality particle beams, to L.B.Golovanov for his constant interest and support, to A.P.Tsvinev and A.Churkin for their help with the vacuum provision, to A.Semenov and Yu.Belikov who kindly lended us computer codes for data acquisition, to P.K.Manyakov for his useful consultations. Authors are grateful also to F.A.Tsimbal, S.Borozdin and O.I.Stolyarov (all from SPbSU) who participated in the multipad anode design.

#### References

- 1. Valiev F.F. et al. JINR Rapid Communications, No.4[50]-91, Dubna, 1991, p.27.
- 2. Baldin A.A. et al. NIM, 1992, A323, p.439.
- ALICE Collaboration at CERN, CERN/LHCC/93-16, LHCC/I 4, 1 March 1993.
- 4. Oba K. et al. IEEE Trans. Nucl. Sci., vol.NS-28, No.1, February 1981, p.705.
- 5. Borozdin S., Feofilov G., Stolyarov O., Tsimbal F., to be published elsewhere.

# КЛАСТЕРИЗАЦИЯ В ПРОЦЕССАХ МНОЖЕСТВЕННОГО РОЖДЕНИЯ ЧАСТИЦ В ЯДРАХ. ДВУХКЛАСТЕРНЫЕ КОРРЕЛЯЦИИ

Н.Ангелов, В.Б.Любимов, Р.Тогоо

Проведен анализ корреляций между кластерами во взаимодействиях (найденных на снимках с 2-метровой пропановой камеры) с образованием по крайней мере двух кластеров. Он показал, что из центральной области вылетают скоррелированные сгустки (кластеры, струи и пр.) с большими поперечными импульсами. Они имеют большие множественности и «температуры», чем кластеры в других областях. Наблюдаются «дальнодействующие» корреляции между кластерами из областей фрагментации мишени и налетающей частицы. Их множественности и «температуры» меньше в сравнении с остальными.

Работа выполнена в Лаборатории высоких энергий ОИЯИ.

Clusterization in Processes of Multiple Particle Production in Nuclei. Two-Cluster Correlations

N.Angelov, V.B.Lyubimov, R.Togoo

The analysis of correlations has been made between clusters in interactions with production, at least, of two clusters (found in photographs from the 2-meter propane chamber). It is shown that correlated bunches (clusters, jets and the others) with large transverse momenta are emitted from the central region. They have larger multiplicities and \*temperatures\* than clusters have in other regions. Long-range correlations between clusters from regions of a target fragmentation and incident particle have been observed. Their multiplicities and \*temperatures\* are smaller in comparison with the rest.

The investigation has been performed at the Laboratory of High Energies, JINR.

Продолжены исследования проблемы кластеризации вторичных частиц, образующихся в неупругих адрон- и ядро-ядерных столкновениях. В предыдущих работах [1—3] были рассмотрены общие характеристики кластеров, в том числе и кластеров в событиях со странными и кумулятивными адронами. Получены результаты по вероятностям кластеризации, температурным характеристикам кластеров и т.д.

В настоящей работе представлены результаты анализа корреляций между кластерами, выделенных в неупругих  $\pi^-p$ -,  $\pi^-$ С-взаимодействиях при  $P_\pi^-=40$  ГэВ/с, а также в AA-столкновениях при P=4,2 ГэВ/с нуклон, найденных на снимках с 2-метровой пропановой камеры Лаборатории высоких энергий ОИЯИ. Для выделения кластеров анализировались взаимодействия с числом вторичных заряженных частиц  $n_\pm \ge 4$ . Данные по AA-взаимодействиям состоят из 6% pC-, 14% dC-, 23% HeC- и 57% CC-столкновений (для событий с числом кластеров  $n_{cl} \ge 2$ ).

Выделение кластеров производилось в пространстве переменных  $b_{ik}' = (m_i m_k/m_0^2) b_{ik}$ , где  $b_{ik} = -(u_i - u_k)^2$ ;  $u_1$ ,  $u_k - 4$ -скорости рассматриваемых частиц;  $m_i$ ,  $m_k$  — их массы;  $m_0$  — атомная единица массы. При этом использовался алгоритм «минимально разветвленного дерева», в котором n частиц рассматриваемого события связываются (n-1) элементами «длины» в пространстве переменных  $b_{ik}'$  так, чтобы суммарная «длина»  $(b_{ik}')$  была минимальной. Затем применялась процедура итераций, в результате которой выделялись наиболее плотные сгущения частиц (кластеры) в этом пространстве.

Таблица 1. Статистика взаимодействий, кластеров и средние характеристики кластеров во взаимодействиях с  $n_{\rm cl} \geq 2$ 

Тип взаимодействий	π <sup>-</sup> p	π <sup>-</sup> C	AA
Число взаимодействий	13560	7700	11020
Число взаимодействий $n_{\rm cl} \geq 2$	4310	4150	3370
Число кластеров	9253	10154	7269
$\langle n_{\rm cl} \rangle$	2,15±0,04	2,45±0,04	2 16±0.04
$\langle n_{\pm} \rangle$	3,28±0,04	3,68±0,04	3.62±0.05
$\langle q \rangle$	-0,01±0,01	0,39±0,01	1.98±0.03
$\langle T \rangle$ (M $_{\odot}$ B)	222±3	217±3	127±2

Для анализа в данной работе использовались взаимодействия с числом кластеров  $n_{cl} \ge 2$ . Статистика событий и кластеров при ведена в табл.1. На этом материале изучались корреляционные функции

$$C(x_{i}, x_{j}) = \rho_{2}(x_{i}, x_{j}) - \rho_{1}(x_{i}) \rho_{1}(x_{j}),$$

Таблица 2. Отношение числа кластеров, дающих положительные корреляции к полному числу кластеров (%)

Тип взаимодействий	$\pi^- p$	$\pi^-C$	AA	
Переменные	%	%	%	
$y_i, y_j$	18,9±0,4	13,1±0,3	12,8±0,4	
$y, P_{\perp}$	$11,8\pm0,4$	$9,7 \pm 0,3$	7,4±0,3	
$y$ , $+\Delta P_{\perp}$	$10,4\pm0,3$	$6,3\pm0,2$	6,3±0,3	
$ \Delta y , P_1$	$10,5\pm0,3$	$6.7 \pm 0.2$	$6.8 \pm 0.3$	
$ \Delta y ,  \Delta P_1 $	15,2±0,5	$10,5\pm0,4$	$11,5\pm0,5$	
y,  ΔP <sub>1</sub>	4,8±0,2	3,1±0,1	3,6±0,2	
$ \Delta y ,  \Delta P_1 $	6,0±0,3	$4,1\pm0,2$	5,0±0,3	
$P_{\perp i}, P_{\perp j}$	$5,9\pm0,2$	$2,9\pm0,1$	8,2±0,3	
y, Ι <b>Λ</b> φΙ	5,1 ±0,2	3,8±0,1	4,5±0,2	
$ \Delta y ,  \Delta \varphi $	$8,6\pm0,4$	7,6±0,3	$8,5\pm0,4$	
$P_{\perp}$ , $ \Delta \varphi $	$8.0 \pm 0.3$	$6,1\pm0,2$	$5,3\pm0,2$	
$ \Delta P_{\perp} ,  \Delta \varphi $	4,3±0,3	$3,5\pm0,2$	$5,8\pm0,4$	

где  $\rho_2(x_i, x_j)$  — двумерные и  $\rho_1(x_i)$ ,  $\rho_1(x_j)$  — одномерные плотности распределений кластеров по переменным  $x_i$  и  $x_j$ , нормированные на единицу.

В качестве переменных  $x_i$ ,  $x_j$  брались величины, характеризующие вылет кластеров:

- а) в продольном направлении продольная быстрота y и  $|\Delta y| = |y_i y_j|$  ( $0 \le y \le y_{\text{max}}$ , где  $y_{\text{max}} = 4.8$  для  $\pi^- p$ -,  $\pi^- C$  и  $y_{\text{max}} = 2.4$  для AA-взаимодействий):
- 6) в поперечном направлении поперечный импульс  $P_{\perp}$ ,  $|\Delta P_{\perp}| = |P_{\perp i} P_{\perp j}|$ ,  $|\Delta P_{\perp}| = |P_{\perp i} P_{\perp j}|$  и  $|\Delta \varphi| = |\varphi_i \varphi_j|$ , где  $\varphi_i, \varphi_j$  углы вылета кластеров в плоскости, перпендикулярной направлению движения первичной частицы  $(P_{\perp}, |\Delta P_{\perp}| \leq 2, 4 \text{ ГрВ/с}, |\Delta P_{\perp}| \leq 4,8 \text{ ГрВ/с})$ . В случаях  $(y_i, y_j)$  и  $(P_{\perp i}, P_{\perp j})$  проводилась симметризация по индексам i и j в двумерных распределениях.

Вычислялись значения корреляционных функции для всех пар переменных. Анализировались: а) области переменных, где  $C(x_i, x_j) > 0$  и  $\Delta C(x_i, x_j) / C(x_i, x_j) < 1$  ( $\Delta C$  — ошибка функций C); б) величины  $N_c = n_{\rm cl}(C > 0) / N_{\rm cl}$ , где  $n_{\rm cl}(C > 0)$  — количество кластеров (комбинаций кластеров), дающих положительные корреляции,  $N_{\rm cl}$  — полное количество кластеров (комбинаций кластеров). Результаты приведены в табл.2.

Из таблицы 2 видно, что:

- 1. Положительные корреляции наблюдаются во всех наборах переменных и типов взаимодействий.
  - 2. В основном  $N_c(\pi^- p) \cong 1,5 \ N_c(\pi^- C) \cong N_c(AA)$ .
- 3. Азимутальные корреляциии практически не зависят от неазимутальной переменной, типа взаимодействия и составляют 5-8%. Корреляционные функции для некоторых пар переменных показаны на рис.1—4. Поведение корреляционных функций  $C(y_i, y_j)$  указывает на существование «дальнодействующих» корреляций в области мишени и налетающего ядра и положительных корреляций в центральной области (рис.1). Корреляции  $C(P_{\perp i}, P_{\perp j})$  свидетельствуют о преимущественном образовании кластеров с близкими поперечными импульсами (рис.2). Видно (рис.3,4) что существуют три области с положительными

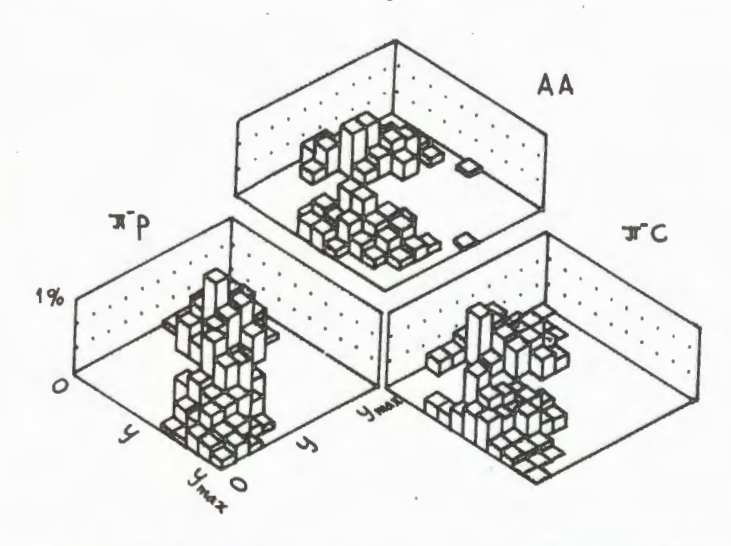


Рис. 1. Корреляционные функции в зависимости от продольных быстрот кластеров

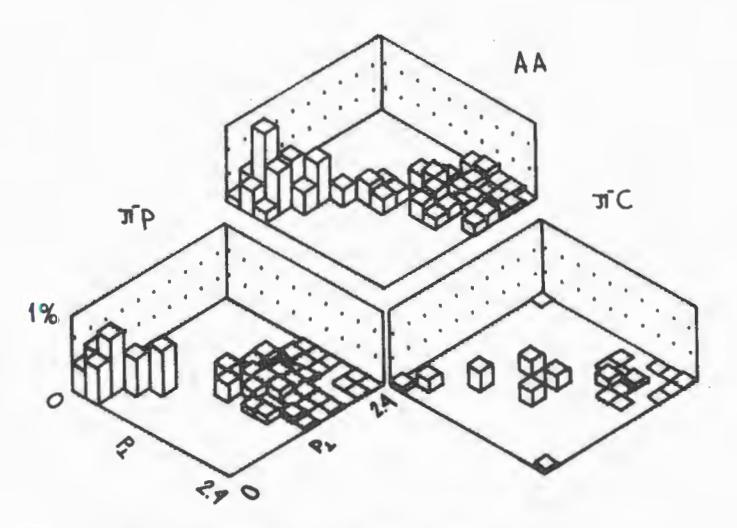


Рис.2. То же, что и на рис.1, но в зависимости от поперечных импульсов

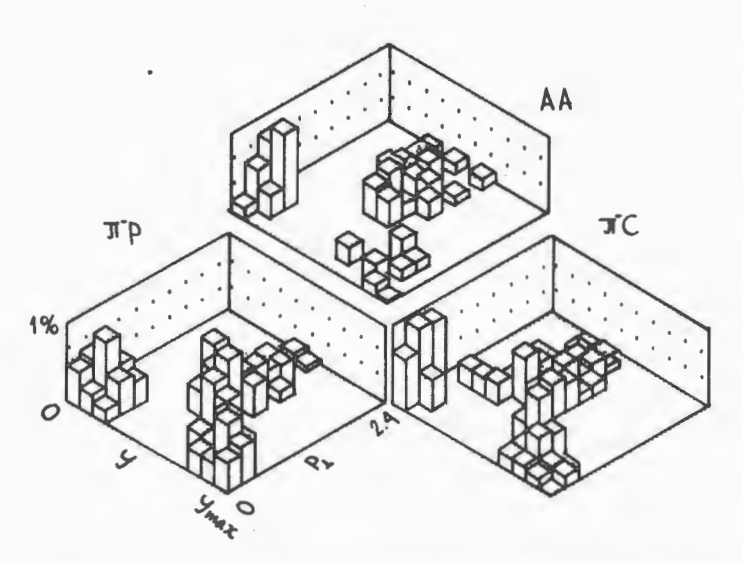


Рис. 3. То же, что и на рис. 1, но в зависимости от продольных быстрот и поперечных импульсов

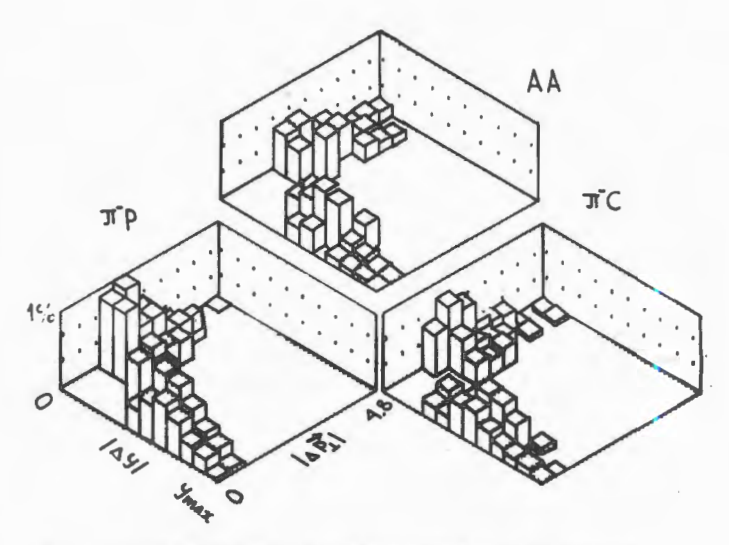


Рис.4. То же, что и на рис.1, но в зависимости от  $|\Delta y|$  и  $|\Delta P_{\perp}|$ 

корреляциями: а) фрагментация мишени —  $0 \le y \le 0.2y_{\text{max}}$  и  $0 \le P_{\perp} \le 0.6$  (ГэВ/с); б) фрагментация налетающей частицы (ядра)  $0.7y_{\text{max}} \le y \le y_{\text{max}}$  и  $0 \le P_{\perp} \le 0.6$  (ГэВ/с); в) центральная область —  $0.3y_{\text{max}} \le y \le 0.6y_{\text{max}}$  и  $0.8 \le P_{\perp} \le 2.4$  (ГэВ/с). При этом примерно в 50% случаев положительные корреляции являются следствием образования кластеров в области мишени и (или) в области фрагментации налетающего ядра. В остальных 50% случаев кластеры вылетают в центральной области с большими поперечными импульсами и под большими углами между ними.

Средние характеристики кластеров — количество частиц  $\langle n_{\pm} \rangle$ , электрический заряд  $\langle q \rangle$ , кинетическая энергия  $\langle T \rangle$  приведены в табл.1. На рис.5—7 показаны их значения в зависимости от продольных быстрот и поперечных импульсов кластеров. Основная закономерность — это рост множественности частиц и их кинетических энергий (в системе покоя кластера) в зависимости от поперечных импульсов кластеров.

Таким образом, анализ корреляций между кластерами во взаимодейтсвиях с образованием по крайней мере двух кластеров показал, что в центральной области вылетают скоррелированные сгустки (кластеры, струи и пр.) с большими поперечными импульсами. Они имеют большие множественности и «температуры», чем кластеры в других обла-

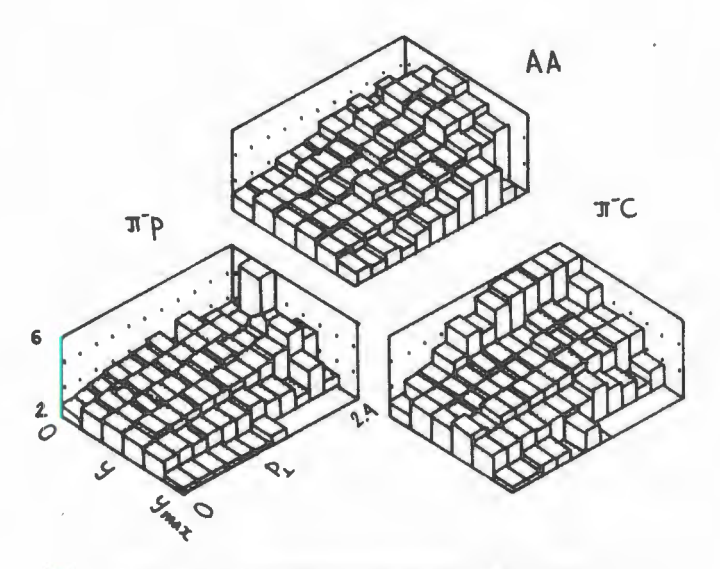


Рис. 5. Зависимость множественности частиц в кластере от у и  $P_{\perp}$ 

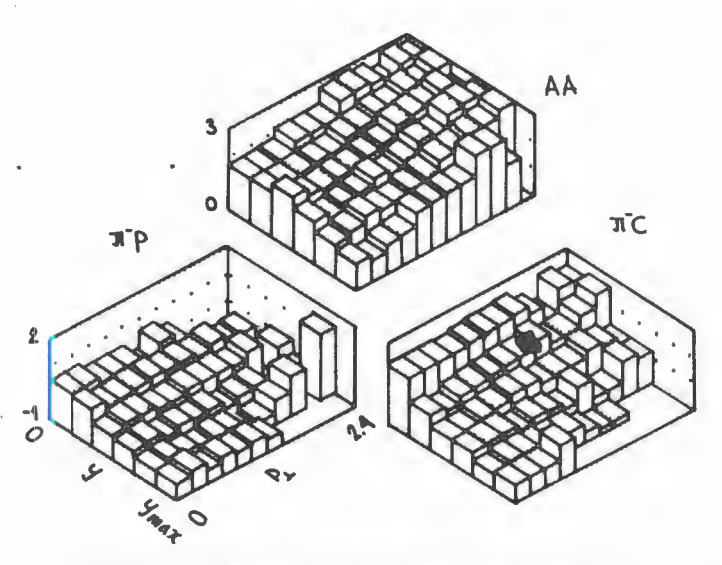


Рис. 6. Зависимость электрического заряда кластера от у и  $P_{\perp}$ 

стях. Наблюдаются «дальнодействующие» корреляции между кластерами из областей фрагментации мишени и налетающей частицы. Их множественности и «температуры» меньше в сравнении с остальными.

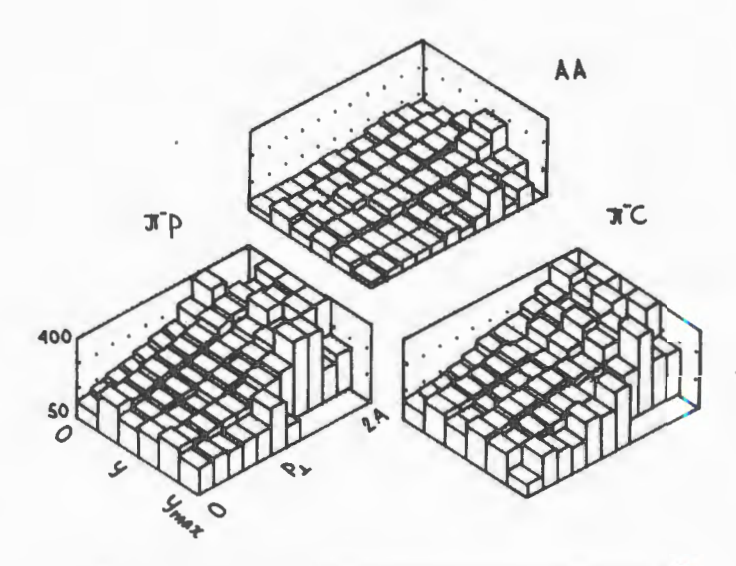


Рис. 7. Зависимость кинетической энергии частиц кластера от у и  $P_{\perp}$ 

## Литература

- 1. Ангелов Н., Любимов В.Б., Toroo Р. ЯФ, 1991, т.54, с.1316.
- Angelov N., Lyubimov V.B., Togoo R. In: X Inter. Seminar on High Energy Physics Problems, Singapore — New Jersey — London — Hong-Kong: World Scientific Publ. Comp. Ltd, 1990, p.117.
- 3. Ангелов Н., Любимов В.Б., Тогоо Р. ЯФ, 1992, т.55, с.2953.

# THE A<sub>LL</sub> ASYMMETRY IN DIFFRACTIVE REACTIONS AND STRUCTURE OF QUARK-POMERON VERTEX

### S.V.Goloskokov, O.V.Selyugin

Theoretical predictions for the behaviour of  $A_{LL}$  asymmetry determined by the pomeron-hadron vertex are done. Strong dependence of the asymmetry on the mass creating quarks and transfer momenta is shown.

The investigation has been performed at the Bogoliubov Laboratory of Theoretical Physics, JINR.

# $A_{LL}$ -асимметрия в дифракционных реакциях и структура кварк-померонной вершины

#### С.В.Голоскоков, О.В.Селюгин

Представлены теоретические предсказания поведения  $A_{LL}$  асимметрии, определяемой структурой кварк-померонной вершины. Показана сильная зависимость величины асимметрии от массы рождающихся кварков и переданного момента.

Работа выполнена в Лаборатории теоретической физики им.Н.Н.Боголюбова, ОИЯИ.

#### 1. Introduction

The spin effects in high energy reactions are still an open problem of perturbative QCD. Like in the framework of the standard perturbative QCD, there is no way to explain many spin phenomena revealed in different processes at high energies.

The spin-flip effects do not exist in the massless limit [1] in hard processes where all quark masses must be omitted. If we do not neglect the quark masses, the spin-flip amplitudes are suppressed as a power of s with respect to the spin-non-flip ones.

The t-channel exchange with vacuum quantum numbers (pomeron) gives a fundamental contribution to high energy reactions at fixed momenta transfer ( $s \rightarrow \infty$ , t-fixed). The calculations of diagrams and their summations are usually performed in the leading logarithmic approximation (see, e.g., [2]). However, the spin-flip amplitudes are absent in this approximation.

As has been intimated, the most part of spin experimental data at high energies are obtained at fixed momenta transfer. So, the theoretical research of the pomeron spin structure is very important. The vacuum t-channel amplitude is usually associated in QCD with the two-gluon exchange [3]. The properties of the spinless pomeron were analysed in [4,5] on the basis of a QCD model with taking account of nonperturbative properties of the theory.

A similar model was used to investigate the spin effects in pomeron exchange. It was demonstrated that different contributions determined by a gluon ladder [6] and quark loops [7] may lead to the spin-flip amplitude growing as s in the limit  $s \to \infty$ . Factorization of the qq amplitude was shown into the spin-dependent large-distance part and the high-energy spinless pomeron. This permits us to define the quark-pomeron vertex and to discuss the results of summation of the pomeron ladder graphs in higher order of QCD. It has been shown that the obtained amplitude leads to the ratio of spin-flip and non-flip amplitudes being perhaps independent of the energy [8]. This result should modify different spin asymmetries and lead to new effects in high energy diffractive reactions which can be measured in future experiments in the RHIC at Brookhaven [9].

## 2. Pomeron and Spin Phenomena

In was demonstrated in the soft momentum transfer region in [6] within the qualitative QCD analysis that the qq spin-flip amplitude growing as s can be obtained in the  $\alpha_s^3$  order. Factorization of the spin-flip amplitude has been shown into the spin-dependent large-distance part (quark-pomeron vertex) and the high-energy spinless pomeron. The quantitative calculations of the spin effects in qq scattering were performed in the  $\alpha_s^3$  order in the half-hard region  $s \to \infty$ , |t| > 1 GeV<sup>2</sup> [10], where the perturbative theory can be used.

It was shown that the quark-pomeron vertex (Fig.1) in the perturbative region has a form

$$\begin{split} V^{\mu}_{qqP}(k,q) &= \gamma_{\mu} u_0(q) + 2m k_{\mu} u_1(q) + 2k_{\mu} k u_2(q) + \\ &+ i \frac{u_3(q)}{2} \varepsilon^{\mu\alpha\beta\rho} k_{\alpha} q_{\beta} \gamma_{\rho} \gamma_5 + i m \frac{u_4(q)}{2} \sigma^{\mu\alpha} q_{\alpha} \,. \end{split} \tag{1}$$

In (1)  $u_i(q)$  are the vertex functions. The term proportional to  $\gamma_\mu$  corresponds to the standard spinless pomeron that reflects the well-known fact

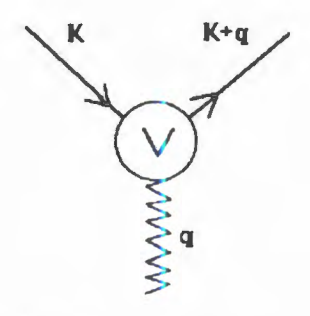


Fig.1. Quark-pomeron vertex

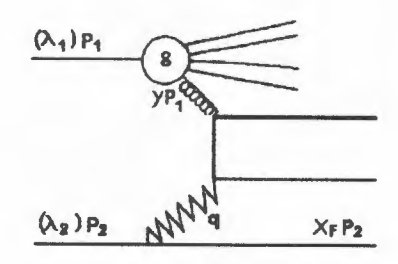


Fig. 2. Diagram for the production of a quark pair in pomeron-hadron interaction

that the spinless quark-pomeron coupling is like a  $C=\pm 1$  isoscalar photon [4]. We use the simple form of the  $u_0(q)$  vertex function

$$u_0(q) = \frac{\mu_0^2}{\mu_0^2 + Q^2}, \qquad q^2 = -Q^2,$$

with  $\mu_0 \sim 1$  GeV introduced in [5]. The functions  $u_1(q) + u_4(q)$  at large  $Q^2$  were calculated in perturbative QCD [10]. Their magnitudes are not very small. Additional spin-flip contributions to the quark pomeron vertex can be connected with instanton effects (see [11], [12] e.g.). The magnitude of these effects is not very well defined because they are model dependent.

Note that the structure of the quark-pomeron vertex function (1) is drastically different from the standard spinless pomeron. Really, the terms  $u_1(q) - u_4(q)$  lead to the spin-flip in the quark-pomeron vertex in contrast to the term proportional to  $u_0(q)$  which is spin-non-flip one. As a result the new terms can modify different spin asymmetries and lead to new effects in high energy reactions.

To show this, let us investigate the quark pair productions in diffractive hadron reactions. This sort of reactions was investigated by different authors (see [13] e.g.). We shall estimate the longitudinal double spin asymmetries in the reaction (Fig.2) as an example. Note that to extract this process, we must detect the final proton with the longitudinal momenta  $p_2' = x_f p_2$ . The angle of this final proton in the c.m.s. is determined by the relation  $\sin(\theta_{p_2'}) = \sqrt{Q^2/(x_f s)}$  and for  $\sqrt{s} = 100 \text{ GeV}$ ,  $Q^2 = 10 \text{ GeV}$ ,  $x_f = 0.7 \text{ we have}$   $\sin(\theta_{p_2'}) \sim 0.04$ .

The resulting asymmetry looks as follows

$$A_{ll} = C_g \frac{(1 - x_f^2) \left\{ 4u_0^2 + Q^2 u_3 \left[ 2u_0 + 4m^2 u_1 + 2m^2 u_2 + m^2 u_4 \right] \right\}}{(1 + x_f^2) \ln \left( s(1 - x_f)/Q^2 \right) \left[ 4u_0^2 + u_3^2 Q^4/2 \right]}. \tag{2}$$

Here

$$G_{g} = \frac{\int_{0}^{1} \Delta g(y) \, dy}{(yg(y)) \big|_{y=0}},$$
(3)

m is the quark mass. For the simple form of the gluon structure function

$$g(y) = \frac{3}{y} (1 - y)^5$$

we have for the coefficient (3)

$$C_g = \frac{\int\limits_0^1 \Delta g(y) \, dy}{3} \, . \tag{4}$$

It is well-known that  $\int_{0}^{1} \Delta g(y) dy \sim 3$  is necessary for the explanation of different spin effects [14]. In this case  $C_g \sim 1$ .

# The A<sub>LL</sub> Asymmetry for the Energy of RHIC and AGS

It is easy to see from (2) that for the standard spinless pomeron that contains the  $u_0$  term, only the asymmetry (2) has a slow  $Q^2$  dependence on the logarithmic term in the denominator. However, we must observe a strong  $Q^2$  dependence in the  $A_{ll}$  asymmetry for the pomeron vertex with the spin-flip part. The resulting asymmetry is equal to zero for  $x_f = 1$ . The  $A_{ll}$  asymmetry for energy of RHIC  $\sqrt{s} = 100$  GeV estimated on the basis of perturbative results for vertex functions for  $x_f = 0.7$  and  $C_g = 1$  is shown in Fig.3. The resulting asymmetry can reach 10 + 12% in the case of large magnitude for the integral (4). As can be seen, from Fig.3, we have an insignificant negative asymmetry for light quarks and positive for quarks with large mass. However, for low energies the asymmetry of light quarks can be sufficiently large.

Similar experiments can be performed at AGS energies ( $\sqrt{s} = 7 \text{ GeV}$ ). In this case we can analyse the production of light and charm quarks. The

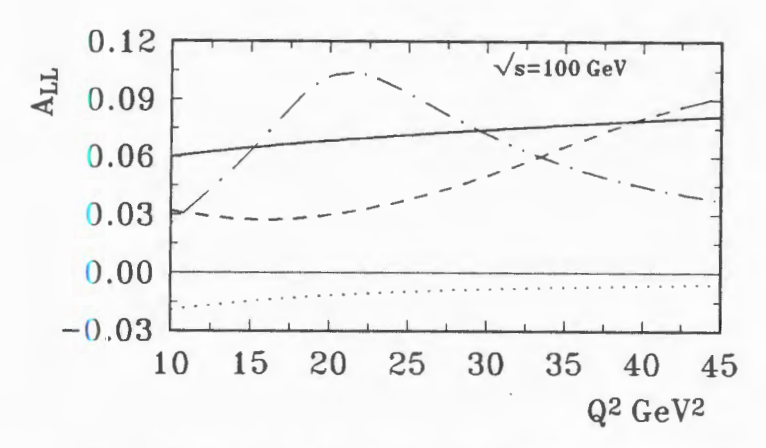


Fig. 3.  $A_{il}$  — asymmetry in the case of the pomeron-hadron interaction at the RHIC energies (for the spinless vertex — solid curve; for the spin-flip vertex and different mass of creating quarks: dotted line — m = 0.005 GeV, dot-dached line — m = 1.3 GeV, short dashed line — m = 4.6 GeV)

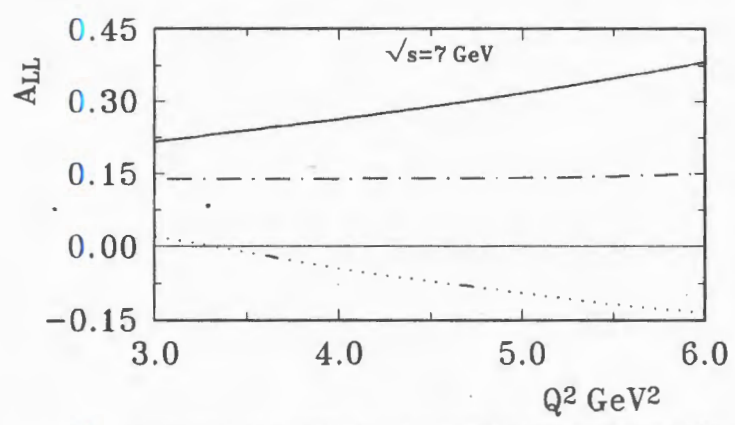


Fig. 4  $A_{II}$  — asymmetry in the case of the pomeron-hadron interaction at the AGS energies (for the spinless vertex — solid curve; for the spin-flip vertex and different mass of creating quarks: dotted line — m = 0.005 GeV, dot-dached line — m = 1.3 GeV)

predictions for the pomeron contribution to the  $A_{LL}$  asymmetries in this case for  $x_F = 0.7$  and  $C_g = 1$  are shown in Fig.4. The asymmetry is large and reaches 40% because in this case we have no large suppression by the  $\ln \left[ s(1-x)/Q^2 \right]$  term in (2). We can see that asymmetry of light quarks can reach 15%. The maximum asymmetry strongly depends on scattering

energies,  $Q^2$  and quark mass. So, for  $\sqrt{s} = 100$  GeV we have the maximum asymmetry at  $Q^2 = 20 + 25$  GeV<sup>2</sup> for the quark mass equal to 1.3 GeV and at  $Q^2 = 45 + 50$  GeV<sup>2</sup> for the quark mass equal to 4.6 GeV.

#### 4. Conclusion

So, the  $A_{LL}$  asymmetry can be measured and the information about the spin structure of the quark-pomeron vertex can be extracted. Therefore, the experiment has been carried out to determine the dependence of asymmetry  $A_{LL}$  on  $Q^2$  for separate mass quark, for example,  $m_q = 1.3$  GeV, or the dependence of asymmetry on the quark mass at separate  $Q^2$ , for example, for  $\sqrt{s} = 100$  GeV,  $Q^2 = 20 + 25$  GeV<sup>2</sup>. This asymmetry can be used for the evaluation in RHIC of

$$\int_{0}^{1} \Delta g(y) \ dy,$$

if the magnitudes of vertex functions  $u_1(q) + u_4(q)$  are known from other experiments or in the opposite case (when the  $\Delta g(y)$  is known) for the determination of the vertex functions  $u_1(q) + u_4(q)$ . This permits one to determine a relative magnitude of the nonperturbative instanton contribution.

Moreover, using the handedness method [15] the final quark-spin correlations with the spin of initial hadrons can be observed.

## Acknowledgement

The authors express their deep gratitude to S.P.Kuleshov and A.N.Sissakian for support of this work and to A.V.Efremov, O.V.Teryaev, M.V.Tokarev and Yu.A.Panebratzev for fruitful discussions.

#### References

- 1. Brodsky S.J., Lepage G.P. Phys. Rev., 1980, D22, p.2157.
- Kuraev E.A., Lipatov L.N., Fadin S.V. Zh. Eksp. Teor. Fiz., 1977, 72, p.377.
- Low F.E. Phys. Rev., 1975, D12, p.163;
   Nussinov S. Phys. Rev. Lett., 1975, 34, p.1286.

- 4. Landshoff P.V., Nachtmann Q. Z. Phys. C-Particle and Fields, 1987, 35, p.405.
- 5. Donnachie A., Landshoff P.V. Nucl. Phys. 1989, B311, p.509
- 6. Goloskokov S.V. Yad. Fiz., 1989, 49, p.1427.
- 7. Goloskokov S.V. Z. Phys. C-Particles and Fields, 1991, 52, p.329; Goloskokov S.V. J. Phys. G: Nucl. Part. Phys., 1993, 19, p.67.
- 8. Goloskokov S.V. Phys. Lett., 1993, B315, p.459.
- 9. Bunce G. et al. Phys. World, 1992, 3, p.1.
- 10. Goloskokov S.V., Selyugin O.V. Yad. Fiz., 1994, 57.
- 11. Dorokhov A.E., Kochelev N.I., Zubov Yu.A. Int. Jorn. Mod. Phys., 1993, A8, p.603.
- 12. Anselmino M., Forte S. Rhys. Rev. Lett., 1993, 71, p.223.
- Berger E.L. et al. Nucl. Phys., 1987, B286, p.704;
   Catani S. et al. Nucl. Phys., 1991, B366, p.135;
   Donnachie A., Landshoff P.V. Phys. Lett., 1992, B285, p.172.
- Soffer J. Proc. of the 10 Int. Symp. on High Energy Spin Phys. (Nagoya, 1992), p.49.
- 15. Efremov A.V., Mankiewicz L., Tornqvist N.A. Phys. Lett., 1992, B284, p.394.

# ВЫХОДЫ И ЭНЕРГЕТИЧЕСКИЕ СПЕКТРЫ ЯДЕР Не, Li, Be B СПОНТАННОМ ДЕЛЕНИИ <sup>248</sup>Cm

М.П.Иванов, И.В.Кузнецов, В.Ф.Кушнирук, В.С.Саламатин, Ю.Г.Соболев, Г.В.Букланов

Измерены выходы и энергетические спектры ядер He, Li и Be в спонтанном делении  $^{248}$ Cm. Для измерений использовался телескоп, содержащий ионизационную камеру для измерения потерь энергии dE и Si(Au)E-детектор. Экстраполированные выходы, наиболее вероятные энергии и ширины энергетических распределений на полувысоте составили  $(2,3\pm0,3)\cdot 10^{-3}$  1/двойное деление,  $(15,6\pm0,3)$  МэВ,  $(10,5\pm0,2)$  МэВ для He;  $(5,91\pm2,11)\cdot 10^{-6}$  1/двойное деление,  $(15,2\pm2,2)$  МэВ,  $(13,4\pm2,0)$  МэВ для Li:  $(1,12\pm0,51)\cdot 10^{-5}$  1/двойное деление,  $(21,1\pm2,8)$  МэВ,  $(13,1\pm2,2)$  МэВ для Be. Наблюдается хорошая корреляция выходов ядер He с  $Z^2/A$  для спонтанно делящихся  $Z^{248,244,242}$ Cm-изотопов, выходы ядер He увеличиваются с увеличением  $Z^2/A$ .

Работа выполнена в Лаборатории ядерных реакций ОИЯИ.

# The Yields and Energy Spectra of He, Li. and Be Nuclei in <sup>248</sup>Cm Spontaneous Fission

#### M.P.Ivanov et al.

The yields and energy spectra of He, Li and Be nuclei accompanyng  $^{248}$ Cm spontaneous fission were measured. A telescop consisting of ionisation chamber for measuring the energy losses dE and a E Si(Au)-detector were used for the measurements. The extrapolated yields, most probable energies and widths are:  $(2.3\pm0.3)\cdot10^{-3}$  1/binary fission,  $(15.6\pm0.3)$  MeV,  $(10.5\pm0.2)$  MeV for He;  $(5.91\pm2.11)\cdot10^{-6}$  1/binary fission,  $(15.2\pm2.2)$  MeV,  $(13.4\pm2.0)$  MeV for Li;  $(1.12\pm0.51)\cdot10^{-5}$  1/binary fission,  $(21.1\pm2.8)$  MeV,  $(13.1\pm2.2)$  MeV, for Be. The good correlation of He nuclei yields with  $Z^2/A$  for spontaneously fissioning  $Z^2/A$ .

The investigation has been performed at the Laboratory of Nuclear Reactions, JINR.

#### Введение

Тройное деление тяжелых ядер, при котором легкая заряженная частица (ЛЗЧ) (Z = 1—8) испускается из области между двумя осколками в момент времени, близкий к разделению ядра, постоянно привле-

кает внимание исследователей. Это связано с тем, что такую ЛЗЧ можно рассматривать как зонд, позволяющий изучать геометрическую конфигурацию ядра и другие характеристики в ходе его деления и таким образом исследовать динамику ядерного деления. Обзор последних результатов, полученных в этой области, дан в работе [1]. Максимальный выход в тройном делении (около 90%) имеют αчастицы с наиболее вероятной кинетической энергией около 16 МэВ (длиннопробежные а-частицы (ДАЧ)). Поэтому выходы ДАЧ (отношение числа испущенных ДАЧ к числу двойных делений), их энергетические и угловые распределения получены для значительно большего числа ядер по сравнению с выходами для других ЛЗЧ. В работе [2] показано, что имеется хорошая корреляция выходов IIA4 с  $Z^2/A$ . Эта корреляция объясняется влиянием оболочечных эффектов в легких осколках. Можно предполагать, что изучение подобных корреляций для ЛЗЧ с Z>2 позволит еще более продвинуться в понимании процесса ядерного деления. Особенный интерес представляет спонтанное деление, в котором влияние оболочек проявляется наиболее сильно.

Экспериментальные данные по тройному делению с эмиссией частиц более тяжелых, чем доминирующая  $\alpha$ —частица, недостаточны из-за их низкого выхода ( $\cong$ < $10^{-5}$  на бинарное деление).

Для ЛЗЧ с Z>2 данные по выходам и энергетическим распределениям получены в основном в экспериментах по вынужденному делению ядер нейтронами и гамма-квантами. Единственным спонтанно делящимся ядром, для которого измерены выходы и энергии ЛЗЧ с Z>2, является <sup>252</sup>Cf. В настоящей работе впервые измерены выходы и энергетические распределения ядер He, Li и Be для спонтанно делящегося ядра <sup>248</sup>Cm.

# Экспериментальная методика

Измерения проводились с использованием (dE-E)-телескопа, схематическое изображение которого приведено на рис.1 (слева). В качестве dE-детектора использовалась ионизационная камера, которая состояла из двух плоских параллельных электродов, имеющих форму круга диаметром 24 см, отстоящих друг от друга на расстоянии 70 мм, и расположенной между ними сетки. Собирающим электродом камеры служила сетка из нихромовой проволоки толщиной 100 мкм, натянутой с шагом 2 мм.

На одном из электродов был закреплен полупроводниковый Si(Au) E-детектор, так, что покрытая золотом поверхность детектора находилась в одной плоскости с поверхностью электрода. Диаметр

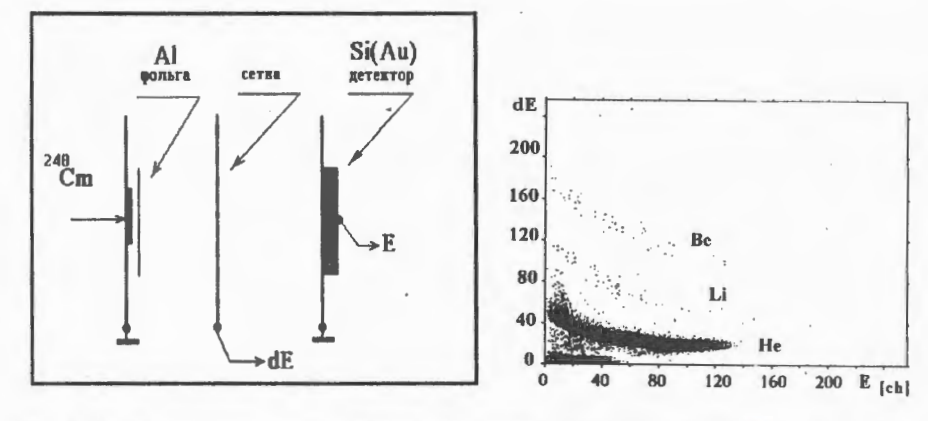
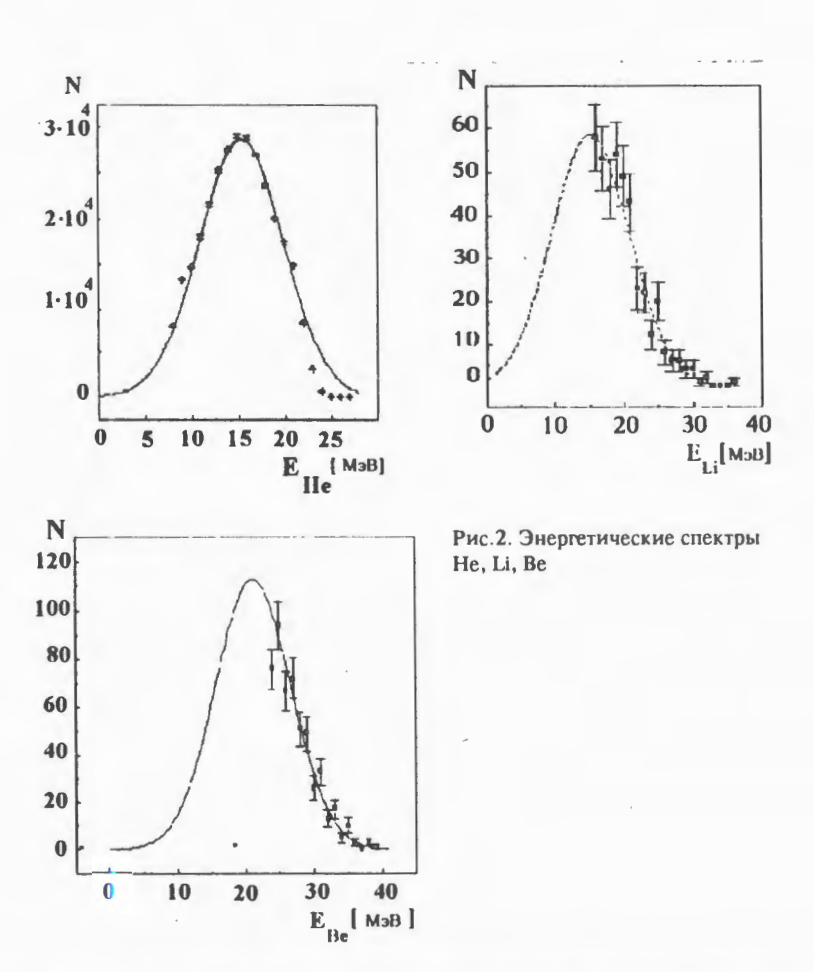


Рис.1. Схема экспериментальной установки (слева), (dE-E)-спектр частиц He, Li, Be (справа).

поверхности и толщина рабочего слоя E-детектора составляли соответственно 50 мм и 200 мкм. На другом электроде камеры устанавливался источник <sup>248</sup>Ст интенсивностью  $10^4$  дел./с. При измерениях ЛЗЧ источник был покрыт Al-фольгой толщиной 28 мкм. Источник представлял собой оксид кюрия  $(96.0\%)^{248}$ Ст,  $3.8\%)^{246}$ Ст, и  $0.2\%)^{244}$ Ст, изготовленный электроосаждением из раствора нитрата кюрия в изобутаноле на подложку из 1.5 мкм  $(710 \text{ мкг/см}^2)$  Ті. Осажденный слой прокаливался при температуре 400%С до получения  $\text{Сто}_2$ . Средняя толщина слоя источника составляла  $150 \text{ мкг/см}^2$  с разбросом по площади 10%. Сверху источник был покрыт слоем углерода толщиной  $30 \text{ мкг/см}^2$ .

Рабочий объем ионизационной камеры заполнялся смесью газов (аргон +10% метана) при давлении 0,2 атм. На сетку подавалось напряжение 400 В. Толщина dE-детектора при этом составляла 2,5 мг/см<sup>2</sup>, что эквивалентно Si(Au)-детектору толщиной 8 мкм. Калибровка dE,E-спектроскопических трактов производилась по энергиям  $\alpha$ —частиц дочерних продуктов распада  $^{226}$ Ra (4,75; 5,46; 5,97 и 7,68 МэВ) из комплекта образцовых источников ОСИАИ и <sup>232</sup>Th (6,06 и 8,78 МэВ). Использовалась стандартная электронная аппаратура с дискриминаторами со следящим порогом и время-амплитудными преобразователями. Накопление и последующая «off-line» обработка информации производилась с помощью персонального компьютера РС АТ 286. Идентификация частиц проводилась выделением зон заселения частиц в двумерной (dE-E)-матрице, представленной на рис.1 (справа). Как видно из рисунка, отсутствие точек между зонами засе-



ления Не, Li, Ве позволяло надежно выделять регистрируемые частицы. Для получения энергетических спектров идентифицированных частиц вводились поправки на потери энергии в Al-фольге в соответствии с [3], при расчете поправок использовались средние значения масс изотопов Li, Ве из [1]. На рис.2 приведены энергетические спектры частиц Не, Li и Ве в спонтанном делении  $^{248}$ Cm, гладкими кривыми представлены результаты  $\chi^2$ -аппроксимации функцией Гаусса, параметры которых даны в табл. 1—3.

# Результаты и обсуждение

В табл. I приведены суммарные выходы изотопов He(Y), наиболее вероятные энергии  $\langle E \rangle$ , ширины распределений по энергии

на половине высоты (ПШПВ) для  $^{248}$ Cm и  $^{252}$ Cf, выходы ЛЗЧ для  $^{242}$ Cm и  $^{244}$ Cm и значения  $Z^2/A$  для каждого нуклида.

Таблица 1. Выход ядер Не

Ядро	$Z^2/A$	Y (×10 <sup>-3</sup> )	<e>, M∋B</e>	пшпв,мэв	Литер.
<sup>242</sup> Cm	38,08	3,89±0,26	_	_	[4]
<sup>244</sup> Cm	37,77	3,18±0,20	_	_	[4]
<sup>248</sup> Cm	37,16	2,3±0,3	15,35±0,3	10,5±0,2	Наст. работа
<sup>252</sup> Cf	38,11	3,21±0,46	15,6±0,2	10,3±0,5	[5]

Число зарегистрированных ядер, выходы и параметры энергетических распределений ядер Li и Be для  $^{248}$ Cm в сравнении с измеренными для  $^{252}$ Cf приводятся в табл. 2 и 3. Выходы отнесены к  $10^4$  ядер He.

Результат, полученный при измерении выхода ядер Не для  $^{248}$ Cm (табл.1), подтверждает отмеченную в [2] зависимость выходов от  $Z^2/A$  для изотопных рядов. Выход ДАЧ почти линейно увеличивается с уменьшением массы изотопа, что можно объяснить увеличением вероятности выхода легкой частицы с увеличением деформации легкого осколка. При этом из измерений следует, что параметры энергетического распределения Не в пределах ошибок эксперимента практически совпадают.

Если следовать такой логике рассуждений, то для выходов ЛЗЧ с Z>2 следует ожидать еще более резкой зависимости от  $Z^2/A$ . Однако в этой области измерения проводились только с  $^{252}$ Cf, и кроме этого имеется большой разброс измеренных параметров, связанный со сложностью измерений и обработки полученных данных. Это видно из результатов, приведенных в табл.2 и 3.

Если считать данные по тройному делению  $^{252}$ Cf с вылетом ядер Li и Be, полученные в работах [8,9], наиболее достоверными, то, повидимому, вывод о более сильной зависимости выходов ЛЗЧ с Z>2 от  $Z^2/A$  подтверждается. Суммарный выход ядер Li на  $10^4$  ядер He для  $^{248}$ Cm примерно в два, а Be в три раза ниже, чем для  $^{252}$ Cf. Из изложенного выше можно сделать вывод о том, что проведение новых более тщательных измерений выходов и энергетических распределений ЛЗЧ тройного деления для более широкого круга спонтанно делящихся ядер позволит существенно расширить наши представления о процессе ядерного деления.

Таблица 2. Выход ядер Li

Ядро	Число частиц	Экстраполир. вых. на 10 <sup>4</sup>	<e>, M∋B</e>	ПШПВ, МэВ	Литер.
<sup>252</sup> Cf	2496	13,2±1,6	20,0±1,0	7.8±2,4	[6]
<sup>252</sup> Cf	3863	29,1±5	18,5±1,0	_	[7]
<sup>252</sup> Cf	_	55±4	_		[8]
<sup>252</sup> Cf	6200	53±6	13,5±1,4	13,8±1,7	[9]
<sup>248</sup> Cm	433	25,7±8,6	15,2±2,2	13,4±2,0	Наст. работа

Таблица 3. Выход ядер Ве

Ядро	Число частиц	Экстраполир. вых. на 10 <sup>4</sup> Не	< <i>E</i> >, МэВ	ПШПВ, МэВ	Литер.
<sup>252</sup> Cf	2264	20,1±2,0	26	13	[6]
<sup>252</sup> Cf	9115	65±7	19,2±1	_	[7]
<sup>252</sup> Cf	_	164±9	_		[8]
<sup>248</sup> Cm	522	48,6±24	13,1±2,2	13,1±2,2	Наст. работа

Авторы благодарны Ю.Э.Пенионжкевичу за постоянную поддержку при проведении эксперимента, Б.И.Пустыльнику за полезные обсуждения, Э.М.Козулину и Ю.В.Лобанову за помощь в работе.

# Литература

- 1. Theobald J. In: Proc. of Int. School-Seminar on Heavy Ion Physics, JINR, E7-93-274, Dubna, 1993, v.1, p.262.
- 2. Wageman C. In: Proc. of Int. Workshop on Dynamical Aspects of Nuclear Fission, JINR, E7-92-95, Dubna, 1992, p.139.
- 3. Northclife L.C., Schilling R.E. Nucl. Data Tables, 1970, v.A7, No.3-4.
- 4. Nobles R.A. Phys.ReV., 1962, v.126, No.4, p.1508.
- 5. Wild J.F. et al. Phys.Rev.C, 1985, v.32, No.2, p.488.
- 6. Cosper S.W., Cerny J., Gatti R.S. Phys.Rev., 1967, 154, p.1193.
- 7. Gazit Y., Nardi E., Katcoff S. Phys.Rev., 1970, C1, p.2101.
- 8. Грачев В.Т. и др. ЯФ, 1988, т.47, вып.3, с.622.
- 9. Dlouhy Z. et al. Report HMI-B, 404, 1989, p.43.